ADVANCING EARTH AND SPACE SCIENCES

JGR Atmospheres

RESEARCH ARTICLE
10.1029/2025JD043679

Key Points:

- Three modes of cloud-boundary layer coupling over the Southern Ocean are identified
- The MYNN-EDMF scheme is advantageous for simulating the decoupled cloud-boundary layer due to its nonlocal mass flux component
- Two key parameters in the MYNN-EDMF scheme dictating shallow clouds formation are identified

Correspondence to:
X.-M. Hu and G. M. McFarquhar,
xhu@ou.edu;
mcfarq@ou.edu

Citation:
Hu, X.-M., McFarquhar, G. M., Zhou, B., & Xue, M. (2025). Performance of conventional and mass-flux PBL schemes for simulating three modes of cloud-boundary layer coupling over the Southern Ocean. *Journal of Geophysical Research: Atmospheres*, *130*, e2025JD043679. https://doi.org/10.1029/2025JD043679

Received 18 FEB 2025
Accepted 21 APR 2025

Author Contributions:
Data curation: Greg M. McFarquhar
Writing – original draft: Xiao-Ming Hu
Writing – review & editing: Bowen Zhou, Ming Xue

Performance of Conventional and Mass-Flux PBL Schemes for Simulating Three Modes of Cloud-Boundary Layer Coupling Over the Southern Ocean

Xiao-Ming Hu[1,2], Greg M. McFarquhar[2,3], Bowen Zhou[4], and Ming Xue[1,2]

[1]Center for Analysis and Prediction of Storms, University of Oklahoma, Norman, OK, USA, [2]School of Meteorology, University of Oklahoma, Norman, OK, USA, [3]Cooperative Institute for Severe and High Impact Weather Research and Operations (CIWRO), University of Oklahoma, Norman, OK, USA, [4]School of Atmospheric Sciences, Nanjing University, Nanjing, China

Abstract Planetary boundary layer (PBL) structure over the ocean and the model capability to simulate such structure are less well-understood than their counterparts over land. In this study, observations and WRF simulations are examined to study the boundary layer structure over the Southern Ocean, focusing on the coupling between the oceanic boundary layer and the cloud layer above. Based on the lower tropospheric vertical profiles and cross-sections, three cloud-boundary layer coupling modes are identified including a coupled mode with a weak positive surface heat flux (type 1), and two decoupled modes in the presence of either a negative surface heat flux driving a shallow stable boundary layer (type 2) or a strong positive surface heat flux (type 3). Numerical simulations are conducted for representative cases of each mode using the conventional YSU PBL scheme without and with the cloud-induced top-down mixing option (referred to as YSUtopdown), as well as the MYNN and the MYNN eddy-diffusivity mass-flux scheme (MYNN-EDMF) that adopts a holistic treatment of mixed-layer thermals and shallow convective clouds. The MYNN-EDMF scheme offers the best representation of the decoupled type 3 mode where its capability to simulate different vertical extents of local mixing and nonlocal mass flux is found to be essential. Two key parameters in MYNN-EDMF dictating shallow cloud formation are also identified. The YSUtopdown scheme develops a deeper boundary layer than the YSU scheme and exhibits more consistency with observations for the coupled type 1 mode. For the decoupled type 2 mode, all four schemes perform similarly well.

Plain Language Summary While the continental planetary boundary layer (PBL) structure and model capability to simulate it are relatively well understood, PBL structure and model performance over oceans in the presence of clouds are less known. In this study, observational data and model simulations are examined to study the boundary layer structure over the Southern Ocean, focusing particularly on the coupling between the surface-based boundary layer and a single cloud layer above. Three cloud-boundary layer coupling modes over the Southern Ocean are identified: 1. Coupled cloud-boundary layer in the presence of weak surface positive flux; 2. Decoupled cloud-boundary layer in the presence of surface negative flux; and 3. Decoupled cloud-boundary layer in the presence of strong surface positive flux. Model simulations were conducted for selected representative cases using both conventional and mass-flux type PBL schemes. The advantages of each scheme are identified for each coupling mode and the root causes are attributed to specific model treatments. The result underscores the advantages of mass-flux PBL schemes in capturing complex cloud-boundary layer interactions with strong surface heat flux, as commonly observed in regions influenced by cold air advection. Such an examination helps to understand model performance and motivates future improvements in Earth system models.

1. Introduction

The planetary boundary layer (PBL) is the lowest part of the atmosphere that is directly influenced by the presence of the earth surface and responds to surface forcings within a short time scale through turbulent mixing. PBL flows exhibit prominent diurnal variations with the daytime and nighttime PBLs often referred to as the convective boundary layer (CBL) and the stable boundary layer (SBL), respectively. Turbulent processes in the PBL dictate the exchange of energy, moisture, and trace gases between the earth surface and the atmosphere, and the subsequent transport and dispersion, playing an essential role in modulating the ambient weather, climate, and air quality. Numerical Weather Prediction (NWP) models normally parameterize turbulent mixing in the atmosphere (both within the PBL and the free troposphere) using a PBL scheme, since their spatial resolutions are usually too coarse to resolve the energetic turbulent eddies. PBL schemes are therefore critical for reproducing the bulk boundary layer structures and vertical profiles in the whole atmospheric column, as well as their subsequent effects on weather and air quality simulations. Uncertainties associated with the PBL schemes remain one of the main sources of inaccuracies in weather and air quality simulations. Many studies (Garcia-Diez et al., 2013; Hu et al., 2010, 2013; LeMone et al., 2013; Nielsen-Gammon et al., 2010; Shin & Hong, 2011; Xie et al., 2012) have evaluated the performance of various PBL schemes, with most of them focusing on continental clear-sky PBL. In comparison, much less is known about the performance of PBL schemes in the presence of clouds and over the ocean (Angevine et al., 2012; Huang et al., 2013; Yang et al., 2019).

Boundary layer and cloud processes are strongly coupled (Deardorff, 1980; Ghate et al., 2015; Lock et al., 2000; Randall, 1980; Yamaguchi & Randall, 2012). The former plays a critical role in the development and dissipation of boundary layer clouds (Yang et al., 2019), while cloud processes may also feedback on the mixed layer structure (van Stratum et al., 2014) as well as boundary layer turbulence (Hu et al., 2011). Cloud top radiative and evaporative cooling can significantly reduce the cloud top temperature and generate negative buoyancy (Finger & Wendling, 1990; Morrison et al., 2011; Pinto, 1998; Solomon et al., 2011; Wang et al., 2001; Zuidema et al., 2005), thus inducing upside-down boundary layers, in which turbulence is dominantly produced aloft and transported downward (Banta et al., 2006; Mahrt & Vickers, 2002), as opposed to the conventional boundary layer where turbulence is mainly generated near the surface and transported upward. Cloud-induced upside-down boundary layers can occur over both mid-latitude (Albrecht et al., 1985; Angevine et al., 2012; Wilson & Fovell, 2018) and high-latitude regions (Hu et al., 2011). The cloud-top-cooling-driven turbulence can be essential to the maintenance (Lilly, 1968), growth and dissipation of clouds (Yang & Gao, 2020). Excessive turbulence at the cloud top may also heat and dry the cloud layer too much, leading to the early dissipation of the cloud (Yang et al., 2019). Whether PBL schemes can handle these boundary layer and cloud processes appropriately remains to be examined.

Conventional PBL schemes often solve equations for the first moment only (first-order closure) or simultaneously solve equation of turbulence kinetic energy (one-and-a-half order closure). They can be generally classified into local and nonlocal schemes (Arya, 2001; Stull, 1988). Local schemes estimate turbulent fluxes at each grid point in space using the values and/or local gradients of atmospheric variables at the same point, whereas nonlocal schemes include turbulent fluxes based on the quantities of atmospheric variables and their gradients at multiple levels in space (Cohen et al., 2015; Hu et al., 2010). Nonlocal turbulent fluxes are usually parameterized using a counter-gradient term (Deardorff, 1966, 1972; Priestley & Swinbank, 1947; Shin & Hong, 2015) or a transilient matrix (Pleim, 2007) with conventional schemes. In CBL where turbulent fluxes are dominated by large eddies that act across many model levels in the vertical, the assumption of local schemes that fluxes depend only on local values and local gradients becomes invalid (Hu et al., 2010). Traditional local schemes (e.g., the Mellor–Yamada–Janjić (MYJ, Janjic, 1990) or the quasi-normal scale elimination (QNSE, Sukoriansky et al., 2005)) tend to underestimate temperature and growth of CBL, while non-local schemes, such as the asymmetrical convective model, version 2 (ACM2, Pleim, 2007), the Yonsei University (YSU, Hong et al., 2006) scheme and the more recently updated Mellor–Yamada Nakanishi and Niino (MYNN, Nakanishi & Niino, 2006) scheme simulate deeper and warmer continental CBLs than MYJ and QNSE (Bright & Mullen, 2002; Clark et al., 2015; Coniglio et al., 2013; Draxl et al., 2014; LeMone et al., 2013; Shin & Hong, 2011; Xie et al., 2012). In addition, nonlocal PBL schemes can reproduce the slightly stable upper CBL with proper treatment/partitioning between local and nonlocal fluxes, while local schemes often predict too thick a superadiabatic layer near the surface and fail to predict a slightly stable upper CBL (Hu et al., 2019; Wang et al., 2016). Whether these conclusions derived over continental cloud-free PBL still apply to cloud-topped boundary layers is unknown. To improve the representation of cloud-topped boundary layers by the YSU scheme, Wilson and Fovell (2018) added extra mixing and entrainment induced by cloud-top cooling in YSU (the resulting scheme is referred to as YSUtopdown). YSUtopdown appears advantageous in reproducing stratocumulus clouds (Lee et al., 2018) and near-surface clouds (Yang et al., 2019), but its performance is not widely examined yet.

Some recent PBL schemes seek a unified representation of both boundary layer and in-cloud turbulence, instead of separate parameterizations by PBL and cumulus schemes (Ching, 1981; Cotton et al., 1995; Golaz et al., 2002; Larson et al., 2012). Besides a more consistent parameterization of atmospheric turbulence in general, the unified treatment also reconciles the coupling between the PBL and cumulus schemes at the cloud base (Zheng, Rosenfeld, & Li, 2021), and is advantageous for modeling constituent transport from the boundary layer to the free atmosphere through cloud venting (Ching, 1981; Cotton et al., 1995; Golaz et al., 2002; Larson et al., 2012). Notably, a class of schemes known as the eddy-diffusivity mass-flux (EDMF) schemes synthesize the gradient-diffusion component from a PBL scheme with the mass flux model from a cumulus scheme to form a unified and holistic representation of boundary layer and shallow cumulus convection (Angevine, 2005; Siebesma et al., 2007; Soares et al., 2004; Suselj et al., 2019; Tan et al., 2018), and the approach has also been extended to include deep convection (Suselj et al., 2022). Within the PBL, the mass flux term replaces the traditional counter-gradient correction term (Deardorff, 1972) to realize nonlocal transport by large eddies. A recently developed MYNN-EDMF scheme by Olson, Kenyon, Angevine, et al. (2019) is shown to be advantageous in the simulation of shallow-cumulus-topped boundary layer (Angevine et al., 2018), which remains a challenge in both NWP and climate models.

The Southern Ocean sits between the Antarctic ice sheet and the rest of the world, and is often covered by low clouds including stratocumulus and cumulus clouds (Jensen et al., 2000; Mace & Protat, 2018b; Muhlbauer et al., 2014). The majority of clouds over the Southern Ocean are quite tenuous and nonprecipitating (Mace & Protat, 2018a). Extratropical cyclones develop in this region frequently (Simmonds et al., 2003), which produce both baroclinic and convective (further divided into closed, open, and disorganized mesoscale cellular convective) clouds in different periphery areas of cyclones and associated fronts (Ahn et al., 2017; Lang et al., 2022; McCoy et al., 2017; Papritz et al., 2015). Thus, the macrophysics and microphysics of the clouds over the Southern Ocean show a strong horizontal variability on the scales of tens of kilometers (e.g., Huang et al., 2015; Lang et al., 2022; McCoy et al., 2017). The cloud cover over the Southern Ocean plays an important role in regulating the global climate due to its strong negative shortwave radiative effect (Hyder et al., 2018; Kay et al., 2016; Trenberth & Fasullo, 2010; Zelinka et al., 2020). However, most general circulation models (GCMs) and NWP models produce large biases in clouds and shortwave radiation when compared to satellite observations (Bender et al., 2017; Bodas-Salcedo et al., 2008, 2014, 2016; Huang et al., 2015; Lang et al., 2018, 2021; Schuddeboom et al., 2019; Williams et al., 2013). Uncertainties in reproducing the interactions between the boundary layer and clouds are at least partially responsible for the biases (Cheng & Xu, 2011; Field et al., 2014; Huang et al., 2014; Truong et al., 2020). Even though incremental model improvements for handling these processes have been achieved, substantial uncertainties still remain (Bodas-Salcedo et al., 2012; Furtado & Field, 2017; Kay et al., 2016; Pelucchi et al., 2021; Ramadoss et al., 2024; Xu & Cheng, 2013). Three field campaigns over the Southern Ocean during austral summer between late 2017 and early 2018 (McFarquhar et al., 2021; Sanchez et al., 2023) collected comprehensive boundary layer data, providing a great opportunity to examine the boundary layer-cloud interaction and to evaluate model capability in reproducing such processes.

In this study, the Weather Research and Forecasting (WRF) model Version 4.5.2 (Skamarock et al., 2021; Skamarock & Klemp, 2008) is used to perform simulations over the Southern Ocean (see Figure 1 for the spatial coverage), focusing on three single cloud layer soundings/cases with different cloud-boundary layer coupling modes. The performance by four PBL schemes, including both conventional and mass-flux type schemes, is examined and explained.

The rest of this paper is organized as follows: In Section 2, observational data, model configurations, and the numerical experiment design are described. In Section 3, cloud-boundary layer coupling modes over the Southern Ocean are first summarized, followed by the performance and root causes of PBL schemes to simulate different cloud-boundary layer coupling modes. The impact of two critical parameters on reproducing the cloud-boundary layer coupling modes is also discussed. Finally, Section 4 contains a summary of the main findings and discussion of the significance and limitations of this study.

2. Data, Model Configuration and Numerical Experiment Design

2.1. In Situ and Remote Sensing Observations Used for This Cloud-Boundary Layer Coupling Study

In situ soundings launched from two ships and released from one aircraft during three field campaigns over the Southern Ocean during austral summer between late 2017 and early 2018 (McFarquhar et al., 2021; Sanchez et al., 2023) are used to examine the cloud-boundary layer structure. The three field campaigns are.

1. The Measurements of Aerosols, Radiation and Clouds over the Southern Ocean (MARCUS) field campaign between 21 October 2017 and 23 March 2018, during which balloons were launched from the Australian

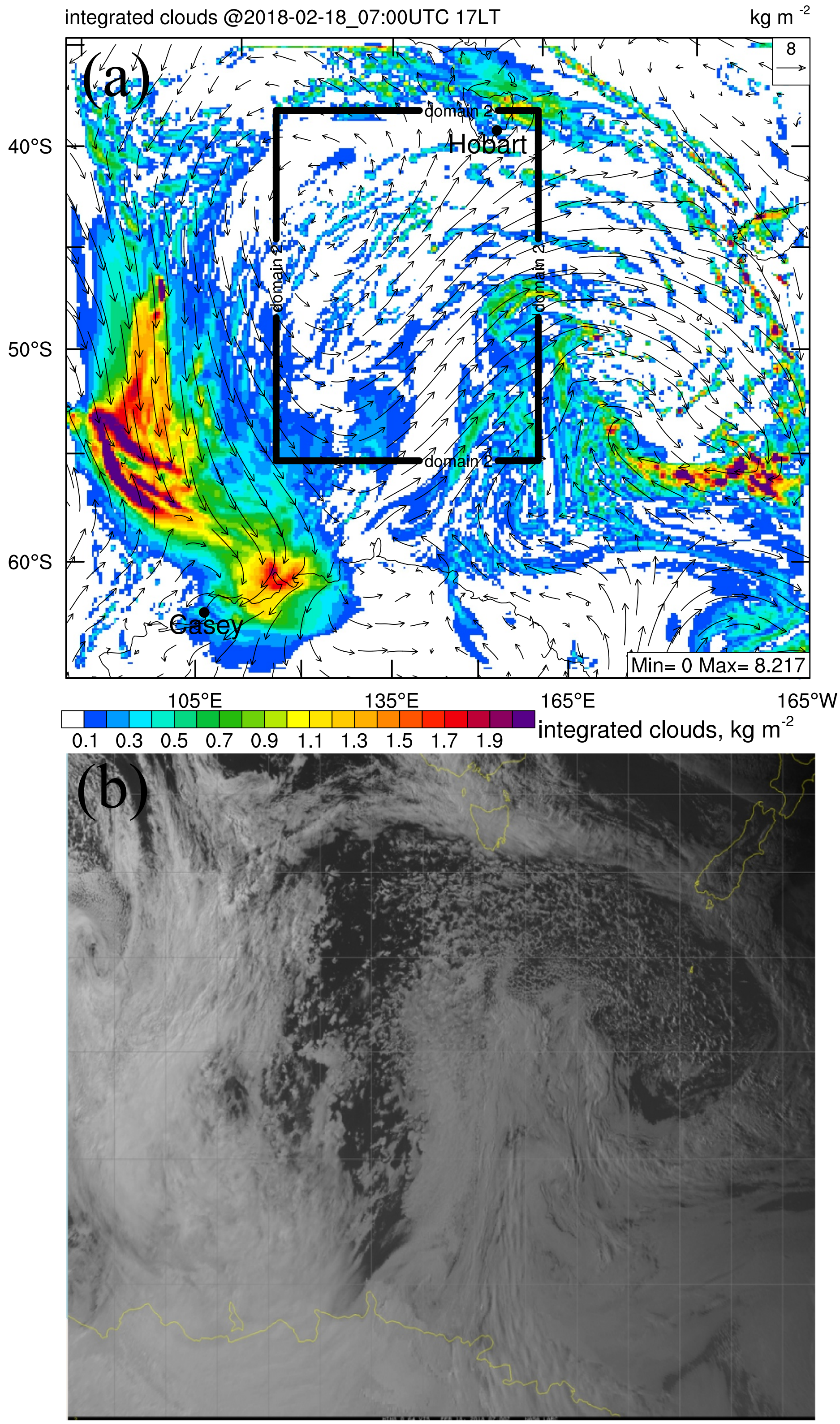

Figure 1. (a) Spatial distribution of column integrated clouds in the first domain simulated by WRF with the MYNN-EDMF PBL scheme at 7 UTC on 18 February 2018, a case examined in detail in Figures 12–20. The one-way nested second domain boundary is marked. (b) Himawari-8 satellite image at the same time retrieved from https://catalog.eol.ucar.edu/maps/socrates.

Antarctic supply vessel Aurora Australis as it transited between Hobart, Tasmania, Australia and the Antarctic stations Mawson, Davis and Casey (Desai et al., 2023; Hu, Lebo, et al., 2023; Xi et al., 2022).

2. The Clouds Aerosols Precipitation Radiation and atmospheric Composition over the Southern Ocean (CAPRICORN) campaign between 11 January to 21 February 2018, during which balloons were launched over the ocean south of Tasmania from the Research Vessel (R/V) Investigator, an Australian Marine National Facility.
3. The Southern Ocean Cloud Radiation and Aerosol Transport Experimental Study (SOCRATES) during 15 January to 26 February 2018, during which dropsondes were released from the NSF–NCAR Gulfstream V (GV) aircraft that flew primarily north-south transects from Hobart, Australia, to within approximately 650 km of the Antarctic coast.

High-quality profiles of temperature, water vapor, wind, and cloud layers (as indicated by ∼100% relative humidity, RH) from these soundings (McFarquhar et al., 2021; Sanchez et al., 2023) are used for model evaluation and classification of the cloud-boundary layer coupling modes.

Remote-sensing data sets from ship-based radar and two satellites (the Cloud-Aerosol Lidar and Infrared Pathfinder Satellite Observation (CALIPSO) and Himawari-8) are used to determine cloud properties (e.g., coverage, vertical distribution) for comparison against simulations. Reflectivity from the marine W-band (95 GHz) cloud radar (Lindenmaier et al., 2018) deployed on the Aurora Australis during the field campaign MARCUS (McFarquhar et al., 2021) is used for examining cloud vertical distribution. Clouds over the Southern Ocean often produce radar reflectivity less than −20 dBZ (Mace & Protat, 2018a, 2018b; Noh et al., 2019). The CALIPSO lidar data, 532 nm total (parallel + perpendicular) attenuated backscatter (Winker et al., 2010) is also used to examine cloud distribution over the Southern Ocean region surveyed by the NSF/NCAR GV aircraft on 18 February 2018. Cloud liquid water path (LWP) during the daytime and cloud top temperature (CLTT) during nighttime from Japan's new-generation geostationary weather satellite Himawari-8 (Smith & Minnis, 2020) are used to examine cloud spatial distribution. LWP can be directly compared with simulated column-integrated cloud water. Given that the LWP retrieval requires satellite radiances at visible and shortwave infrared wavelength channels (Wang et al., 2024), retrieved LWP is only reliable for clouds occurring during daytime. During nighttime, only the CLTT derived from Himawari infrared channels is used.

2.2. Model Configurations

The boundary layer structure is first examined with soundings from the three Southern Ocean field experiments and similar soundings/cases are grouped. The WRF model version 4.5.2 (Skamarock et al., 2021; Skamarock & Klemp, 2008) is used to perform simulations with two one-way nested domains using 15- and 3-km horizontal grid spacings centered on the Southern Ocean (see Figure 1 for domain coverage). A total of nine sounding cases are examined (summarized in Figures 2–4), including 1 December 2017, January 10, 21–23 March 2018 detected by the Aurora Australis from the MARCUS experiment, and 17–18 February 2018 detected by the RV Investigator/GV aircraft from the CAPRICORN and SOCRATES experiments. For 21–23 March 2018, the inner domain is shifted east to ensure it can encompass the soundings from the Aurora Australis. The prevailing cloud type over the area of investigations on these days are stratiform clouds or scattered shallow cumulus clouds, as revealed by the Himawari-8 satellite images and simulations (e.g., Figure 1). These cases are representative of single-layer clouds sampled during the three field campaigns. During these cases, the same boundary layer structure stayed for at least 1–2 days. Thus, the models are more likely to reproduce such a boundary layer structure than some fast-evolving, short-lived cases. The WRF simulations are initialized at 00 UTC of the previous day of each sounding to allow at least 24-hr model spin-up before being evaluated against observations. The nine sounding cases are categorized into three cloud-boundary layer coupling modes (Hu et al., 2021) as assembled in Figures 2–4 respectively and are described in Section 3. These cases are based on individual soundings. Two soundings collected by NSF–NCAR GV aircraft dropsondes on 18 February 2018 are ∼700 km apart. Three cases (1 December 2017; 10 January 2018; 18 February 2018) representing each mode are selected for detailed analysis.

The WRF simulations use the ERA-Interim data of 0.7° resolution (Dee et al., 2011) for initial and boundary conditions, which follows previous studies focusing on boundary layer structures using the WRF model (Hu et al., 2019; Huang et al., 2014; Lang et al., 2021). Given that our 15-km grid spacing outer grid is rather large (about 4,500 × 4,000 km^2) and our time integrations are only two days, the solutions on the nested 3 km grid that

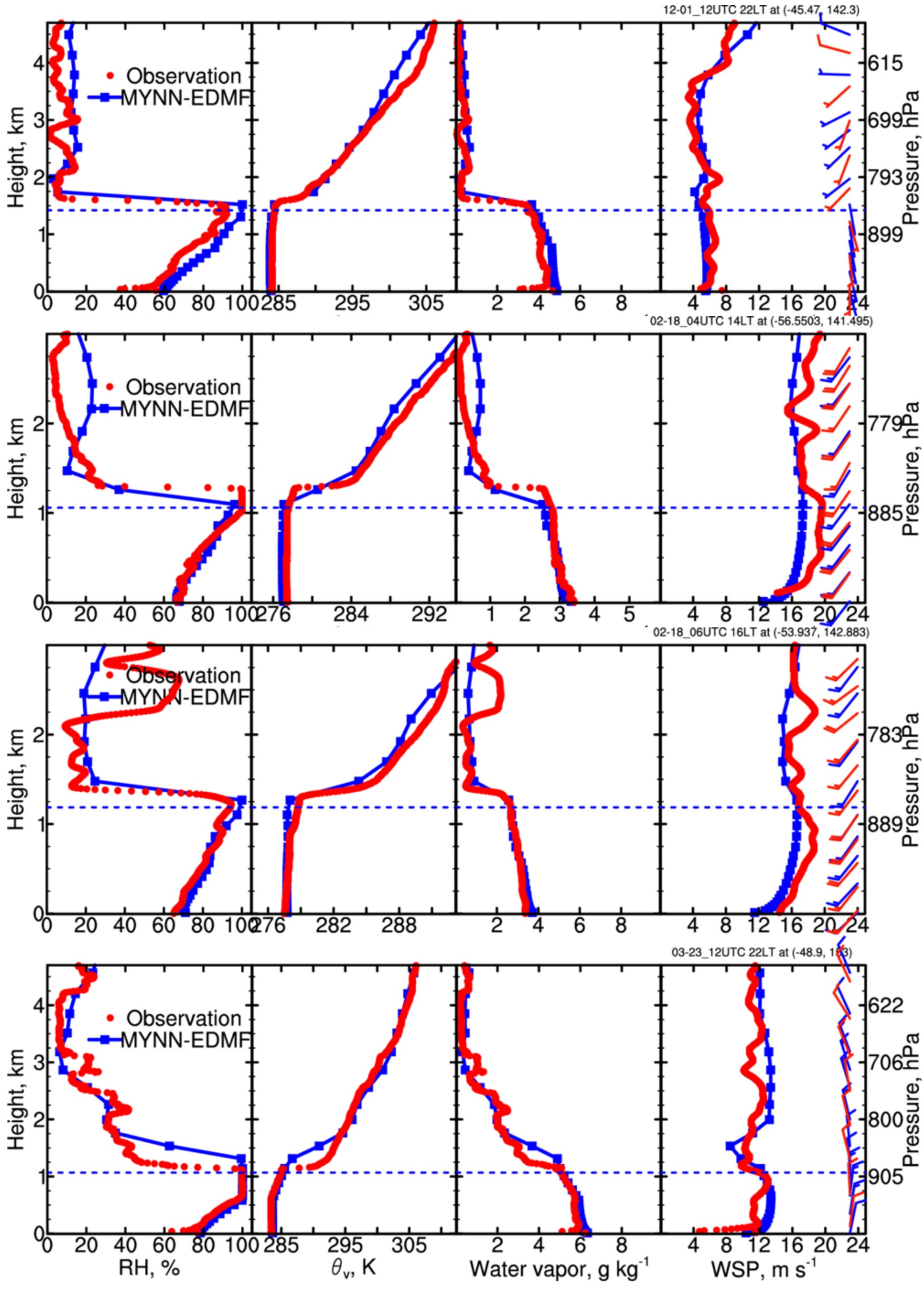

Figure 2. Simulated and observed profiles of (left to right) RH, virtual potential temperature (θ_v), water vapor mixing ratio, and wind speed (WSP)/vectors for (top to bottom) four coupled cloud-boundary layers on 1 December 2017, 18 February 2018, 23 March 2018, detected by the Aurora Australis, R/V Investigator, NSF/NCAR GV, and Aurora Australis respectively. Simulated PBL top is marked by a dashed line. Sounding latitude/longitude are marked at top-right corner.

10.1029/2025JD043679

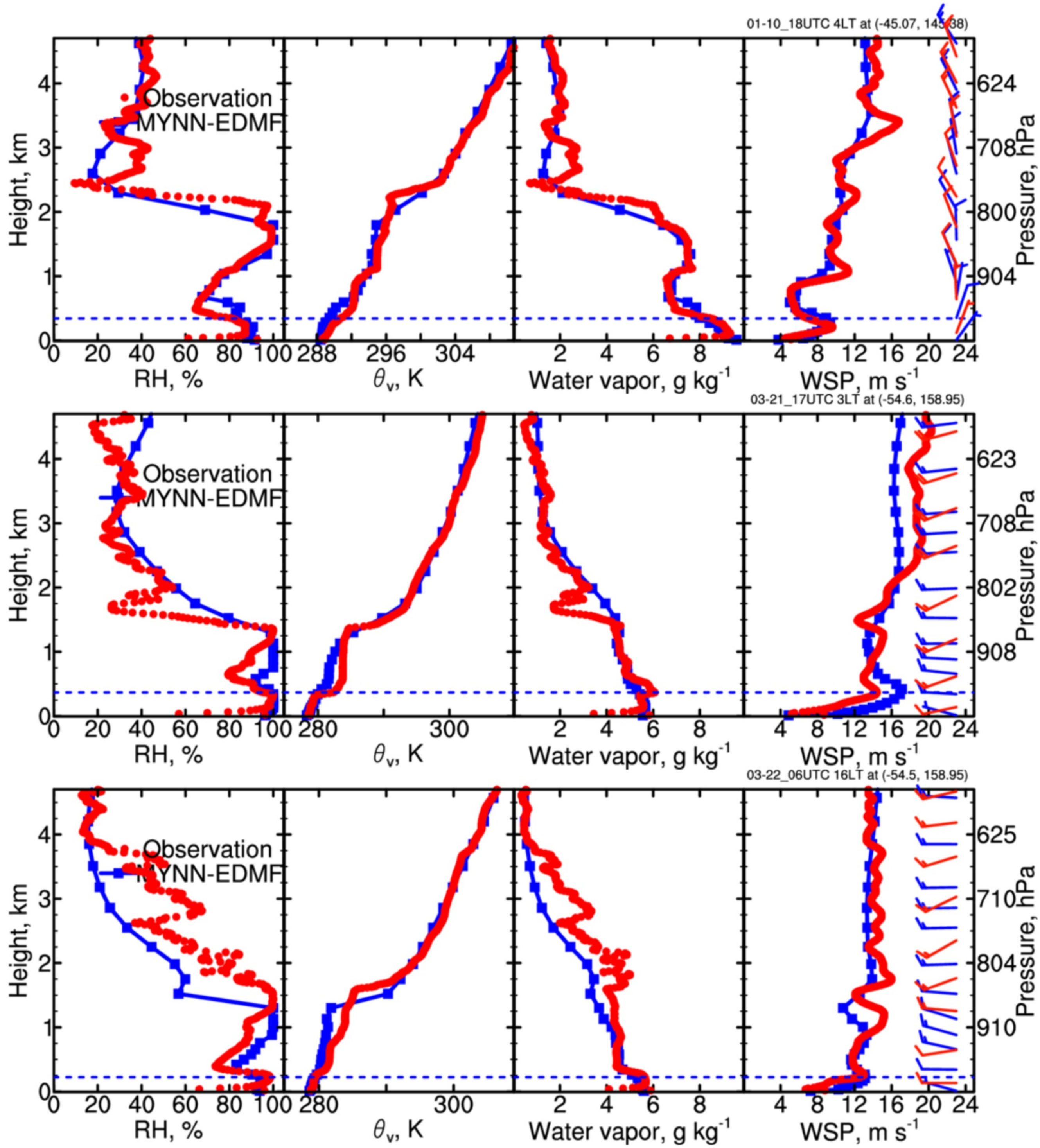

Figure 3. Simulated and observed profiles of (left to right) RH, virtual potential temperature (θ_v), water vapor mixing ratio, wind speed (WSP)/vectors for (top to bottom) three decoupled cloud-boundary layers in presence of surface negative sensible heat flux on 10 January 2018, 21 March, and 22 March 2018, detected by the Aurora Australis. Simulated PBL top is marked by a dashed line. Sounding latitude/longitude are marked at top-right corner.

we are most interested in are not very sensitive to the reanalysis data used to provide the lateral boundary conditions. Both domains use 48 stretched vertical levels topped at 100 hPa with 17 layers in the lowest 1 km above the surface to resolve boundary layer processes. For each case, four sensitivity experiments were conducted with

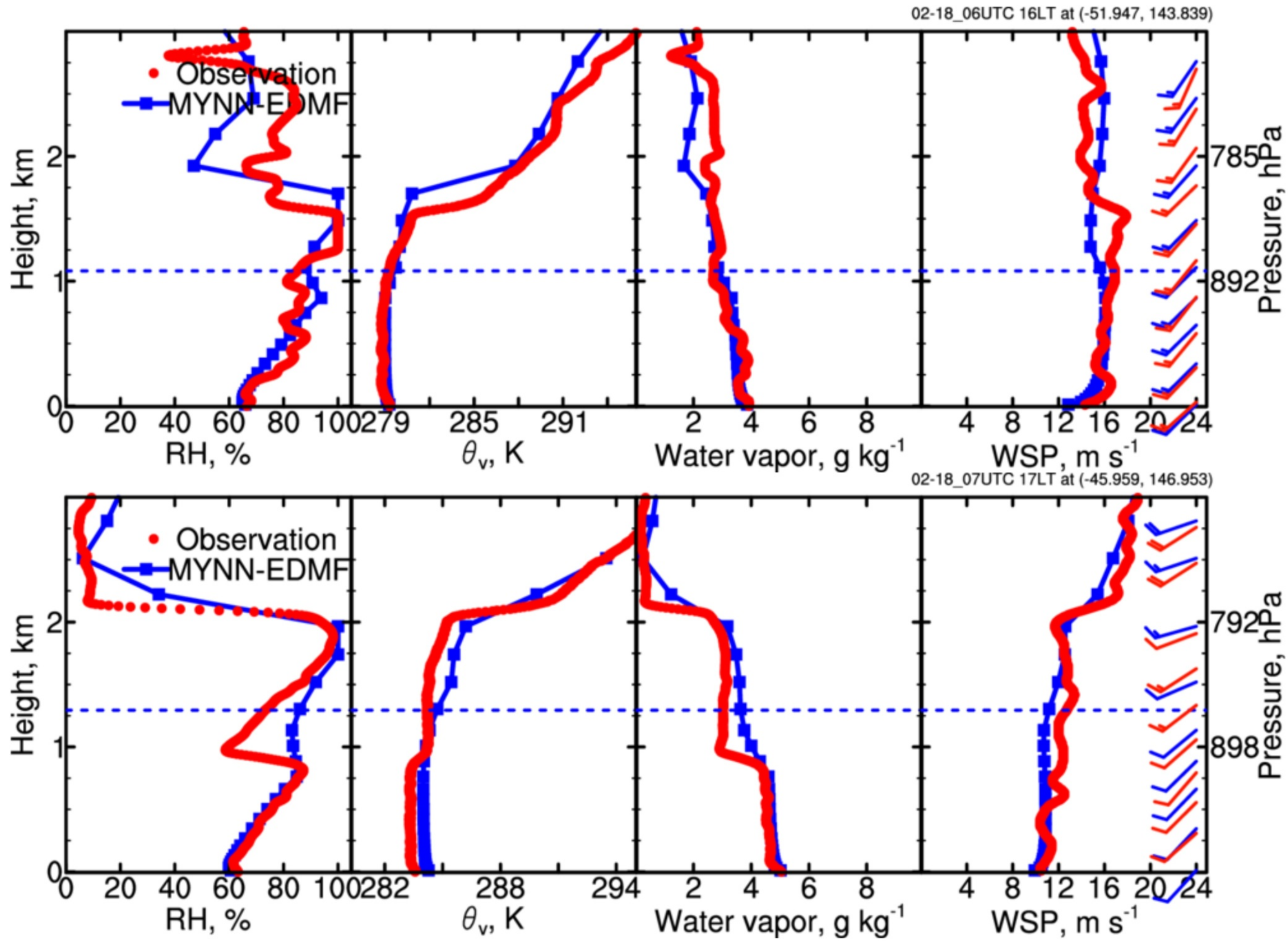

Figure 4. Simulated and observed profiles of (left to right) RH, virtual potential temperature (θ_v), water vapor mixing ratio, and wind speed (WSP)/vectors for (top to bottom) two decoupled cloud-boundary layers in presence of surface positive sensible heat flux at 6 and 7 UTC on 18 February 2018, detected by NSF/NCAR GV dropsondes. Simulated PBL top is marked by a dashed line. Sounding latitude/longitude are marked at top-right corner.

varied PBL schemes, while other physics parameterizations were kept the same, including the revised MM5 Monin-Obukhov surface layer scheme (Jiménez et al., 2012), the Rapid Radiative Transfer Model for GCMs (RRTMG) longwave and shortwave radiation scheme (Iacono et al., 2008), the Morrison microphysics scheme (Morrison et al., 2009), and the scale-aware Grell-Freitas cumulus scheme (Grell & Freitas, 2014) that is used on both the 15-km outer domain and the 3-km inner domain for deep moist convection. Four PBL schemes are examined in this study, including three conventional and one EDMF-type schemes, that is, the YSU scheme, YSU with cloud-induced top-down mixing (YSUtop-down), the MYNN scheme, and the MYNN-EDMF scheme which extends the MYNN scheme by including a nonlocal mass flux term.

Table 1
Configurations for Sensitivity Simulations With the MYNN-EDMF PBL Scheme Varying the Empirical Coefficient for the Fractional Entrainment of Individual Plumes (c_ε) and Capping Height of Individual Convection Plumes (h_p)

MYNN-EDMF simulations	h_p(m)	c_ε(m s^{-1})
Control	3,500	0.33
Experiment 2	500	0.33
Experiment 3	2,500	0.33
Experiment 4	4,500	0.33
Experiment 5	3,500	0.2
Experiment 6	3,500	0.55
Experiment 7	3,500	0.9

2.3. Parameter Sensitivity Experiments With MYNN-EDMF

To understand the behavior of the mass flux treatment of MYNN-EDMF, additional parameter sensitivity experiments are conducted by varying two key parameters in the mass flux treatment (summarized in Table 1). The two parameters are identified based on previous studies and recommendation by the MYNN-EDMF developer (personal communication with J. Olson, Feb. 2023). In a previous study (Berg et al., 2021), the sensitivity of simulated turbine-height winds to MYNN-EDMF parameters was examined.

Simulations in a fully developed convective boundary layer were shown to be most sensitive to c_ε, an empirical coefficient in parameterizing the fractional entrainment of individual plumes (ε_i), which is given by

$$\varepsilon_i = \frac{c_\varepsilon}{w_i d_i}, \tag{1}$$

where w_i and d_i are the updraft speed and plume diameter of the i th updraft (Tian & Kuang, 2016). c_ε is set to 0.33 m s^{-1} in the default MYNN-EDMF in WRF version 4.5.2. Berg et al. (2021) noted that c_ε is determined empirically and may vary on the order of 0.1 m s^{-1}. In this study, it is allowed to vary among 0.2, 0.55, 0.9, and 0.33 m s^{-1} (see Table 1).

The second parameter examined is related to the capping height of individual convective plumes. To constrain only parameterizations of shallow cumulus clouds and not overlapping too much with mid-level and deep convection, which are handled separately by the cumulus scheme, the mass flux of individual plumes is limited to occur only within 3,500 m above the surface (h_p) in the MYNN-EDMF scheme in WRF version 4.5.2 (personal communication with J. Olson, 2023). The limit is imposed on the updraft velocity w_i as

$$w_i^*(z) = w_i(z)\exp\left(-\frac{\max(z - \min(z_i + 2000, h_p), 0)}{1000}\right), \tag{2}$$

where w_i^* is the vertical velocity of the ith updraft after the capping limit is imposed, z_i is the boundary layer depth. For example, for $h_p = 500$ m, w_i^* at $z = 1{,}000$ m shall be limited to $\exp(-0.5)\,w_i$ or $0.6w_i$, where w_i is obtained from the bulk plume equations. Our previous simulations of clouds over the Amazon region appear quite sensitive to h_p (Hu, Huang, et al., 2023). In our sensitivity experiments here, h_p is allowed to vary among 500, 2,500, and 4,500 m.

3. Results

3.1. Identification of Three Cloud-Boundary Layer Coupling Modes

The boundary layer structure reflected by the soundings from the three Southern Ocean field experiments (i.e., MARCUS, CAPRICORN, and SOCRATES) are first visually examined and simulated for the nine cases described in Section 2.2. The WRF simulations with the MYNN-EDMF PBL scheme capture the main boundary layer and cloud layer structure in terms of profiles of potential temperature, water vapor mixing ratios, wind speed/vectors, and RH for these cases, even though biases exist for certain details (Figures 2–4). The simulated PBL tops are marked in Figures 2–4 to aid classification. The classification of cloud-boundary layer coupling modes is conducted based on the boundary layer height z_i and the cloud layer, while also taking into consideration the surface sensible heat flux H_s. The boundary layer height z_i simulated by MYNN-EDMF is defined as the level where potential temperature first exceeds the minimum potential temperature within the boundary layer by 1.5 K (often referred to as the 1.5-theta-increase method). When applied to observed temperatures, this method has been shown to produce z_i estimates that are unbiased relative to profiler-based estimates (Nielsen-Gammon, 2008). For stable boundary layers, the PBL top is defined as the location where turbulent kinetic energy (TKE) drops below the max of 0.02 m^2 s^{-2} and 1/40 of first layer TKE following recommendation by Pichugina and Banta (2010). The cloud layer is defined as the altitude where RH exceeds 0.95. Surface sensible heat flux H_s is obtained from WRF simulations with the MYNN-EDMF PBL scheme. The nine cases are categorized into three cloud-boundary layer coupling modes, which are

1. The coupled cloud-boundary layer under weakly positive H_s (~20 W m^{-2}) as shown in Figure 2;
2. The decoupled cloud-boundary layer in the presence of negative H_s and a shallow SBL as shown in Figure 3; and
3. The decoupled cloud-boundary layer in the presence of relatively large H_s (>40 W m^{-2}), higher clouds, and a thick mixed layer as shown in Figure 4.

For type 1 mode, the boundary layer top is located at about 1–1.4 km, coinciding with the cloud base height where RH reaches 100%, indicating a cloud-topped boundary layer (Figure 2). In this mode, the clouds and the underlying boundary layer are considered coupled. For type 2 mode, a shallow SBL (~300 m thick) develops under negative H_s, while a separate/decoupled cloud layer is maintained at 1–2 km above the surface (Figure 3). The characteristic low-level jets (LLJs) develop with a jet nose located at the top of SBL at less than 300 m above the surface. This LLJ can be explained by the inertial oscillation theory, according to which wind oscillation amplitude peaks at the top of the boundary layer (Blackadar, 1957; Klein et al., 2016; Shapiro & Fedorovich, 2010). For type 3 mode, a thick surface-based boundary layer (∼1 km thick) develops while a separate/decoupled cloud layer is maintained at 1.2–2 km above the surface (Figure 4). The cloud base is higher than the PBL top by more than ∼200 m. In the following, three representative cases (1 December 2017; 10 January 2018; 18 February 2018), one for each mode, are selected for detailed analysis, WRF simulations with different PBL schemes are examined in terms of the causes for reproducing (or not reproducing) the three cloud-boundary layer coupling modes.

3.2. Coupled Cloud-Boundary Layer in the Presence of Weakly Positive H_s

On 1 December 2017, a cyclone developed over the Southern Ocean off Casey. To the northeast of the cyclone, a low-level ridge at 800 hPa developed and penetrated to the southwest of Hobart (Figure 5f). When the Aurora Australis approached Hobart on its trip back from Davis, it passed a region with southerly winds (Figure 2) on the northeast side of the ridge, thus cold air advection occurred (Figure 5a) and thin scattered clouds developed in the region as indicated by the distribution of cloud top temperatures detected by Himawari-8 (Figure 5h). In the presence of cold air advection over the relatively warmer ocean (creating near-surface instability as indicated by temperature gradient, SST-T2, Figure 5d), there was positive surface sensible heat flux of ∼20 W m^{-2} (Figure 5b) and latent heat flux of >80 W m^{-2} (Figure 5g) at the sounding location. The four PBL schemes simulate a cloud-topped boundary layer at 12 UTC (22 local time), reproducing the coupled cloud-boundary layer mode (Figure 6). The cross-sections of cloud hydrometers in Figure 7 more clearly illustrate the coupled cloud-boundary layer: the simulated boundary layer top passes through the scattered clouds over 49.5–39.5°S, a region as wide as more than 1,000 km. Cloud radar reflectivity data between 46.1°S and 45.3°S (when the Aurora Australis sailed during 05–16 UTC) verify the cloud layer at an altitude between 0.9 and 1.7 km in the region (Figure not shown). The MYNN-EDMF reproduces the boundary layer top gradients of RH, potential temperature, and water vapor with the best agreement, particularly in terms of their altitude at this sounding location (Figure 6). The YSU scheme underestimates the boundary layer height by ∼300 m, leading to an overestimation of water vapor mixing ratios by ∼1 g kg^{-1} in the boundary layer (Figure 6). Consequently, it overestimates RH in the boundary layer and the simulated boundary layer top clouds are lower than observations by ∼300 m (Figure 6). With the additional top-down mixing from cloud-top cooling, YSUtopdown simulates a deeper boundary layer (Figures 6 and 7), likely due to the enhanced entrainment process associated with the additional top-down mixing facilitating the boundary layer growth. As a result, YSUtopdown shows better agreement with the sounding profiles than YSU. The moist bias of water vapor of 1 g kg^{-1} in the boundary layer from YSU is reduced and the boundary layer top cloud is elevated close to the altitude of the observed clouds (Figure 6). These results are consistent with previous studies showing that the YSU scheme underestimates entrainment near the top of the cloud-topped boundary layer and YSUtopdown can alleviate such an underestimation (Ghonima et al., 2017; Wilson & Fovell, 2018).

3.3. Decoupled Cloud-Boundary Layer in the Presence of Negative H_s With a Shallow Surface-Based BL

On 9–10 January 2018, a stationary cyclone persisted over the Southern Ocean off Casey and northwesterly flow and thus warm air advection persisted between Casey and Australia. When the warm air impinged on the colder air mass (Figure 8a), a baroclinic cloud zone formed (Figure 8e), as confirmed by the Himawari-8 cloud top temperature (Figure 8h). To the northeast of the baroclinic cloud zone, a high-pressure ridge at 500 hPa developed and penetrated to the southeast of Hobart and consequently a surface anticyclone developed over the ocean southeast of Hobart (Figure 8f) when the Aurora Australis approached Hobart on its trip back from Casey on Jan. 10. Northerly offshore winds prevailed over the ocean to the south and southwest of Hobart (Figures 2 and 8), where it was sampled by the soundings from Aurora Australis (Figure 9). Since the air over Australia is relatively warmer, the northerly winds led to warm air advection. In the presence of warm advection over the colder ocean, there was weak latent heat flux (<20 W m^{-2}, Figure 8g) and negative surface sensible heat flux of ∼−20 W m^{-2} (Figure 8b). In the presence of such negative heat flux and atmospheric stability as indicated by SST-T2 (Figure 8d), the near-surface turbulence was suppressed, and the boundary layer was shallow and stable (200–300 m). Because of the attenuation of near surface turbulent mixing, winds above the stable boundary layer accelerated and a LLJ formed at the top of the boundary layer (Figure 9) according to the inertial oscillation theory

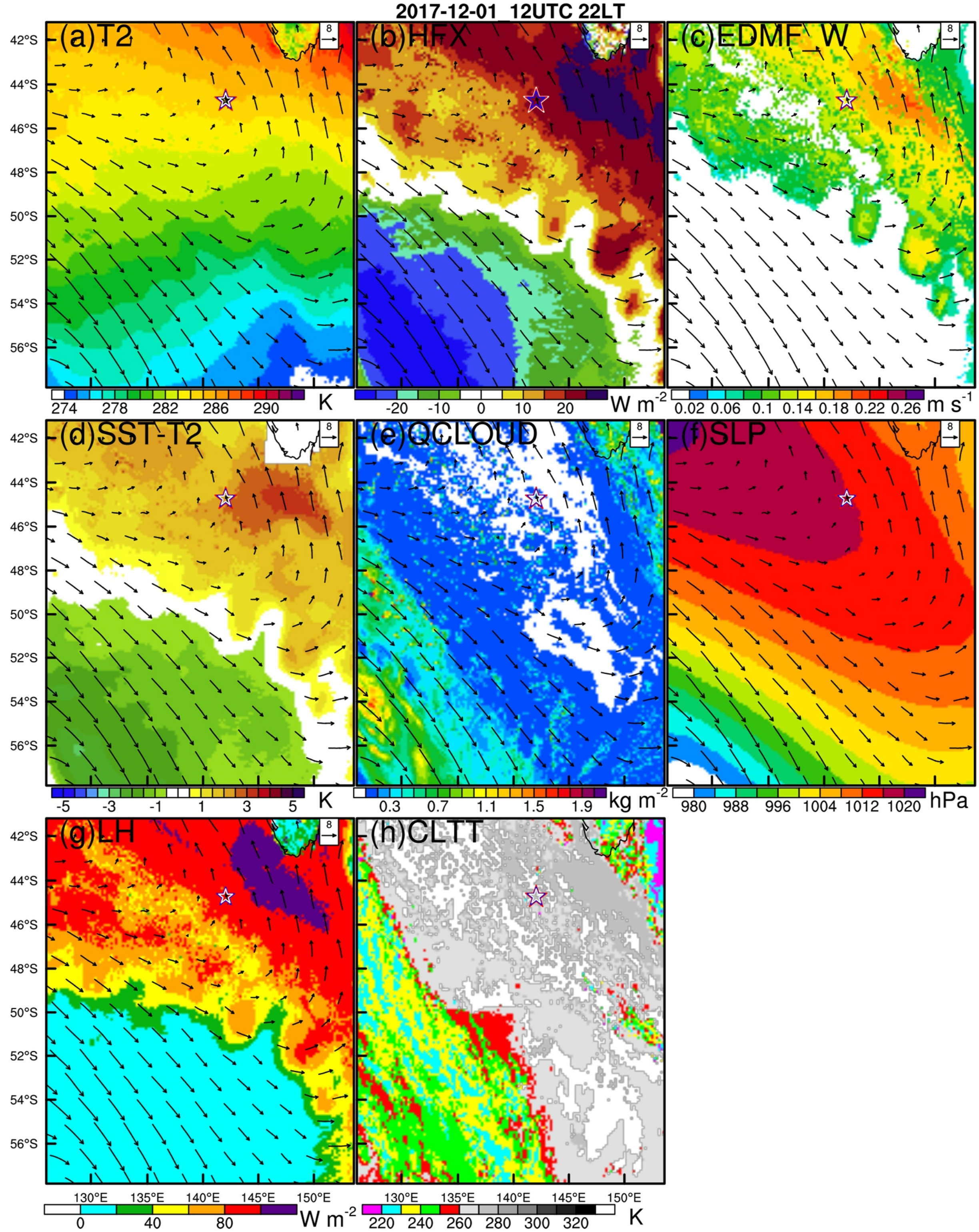

Figure 5. Spatial distribution of simulated (a) T2, (b) sensible heat flux (HFX), (c) mass flux vertical velocity (EDMF_W) at the first model layer above ground, (d) difference between sea surface temperature and temperature at 2 m (SST-T2), (e) integrated cloud water, (f) sea level pressure (SLP), (g) latent heat flux (LH), and (h) cloud top temperature (CLTT) from the Himawari satellite at 12 UTC on 1 December 2017. The location of the Aurora sounding is marked by a star.

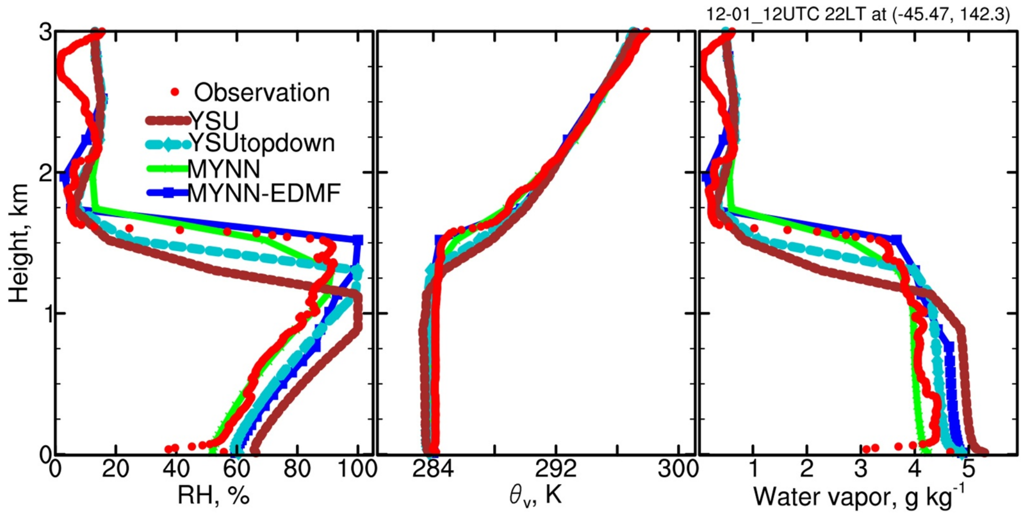

Figure 6. Profiles of (left to right) RH, virtual potential temperature (θ_v), Water vapor mixing ratio in a coupled cloud-boundary layer at 12 UTC on 1 December 2017 observed by Aurora sounding and simulated by WRF with four PBL schemes. Sounding latitude/longitude are marked at top.

(Blackadar, 1957; Klein et al., 2016; Shapiro & Fedorovich, 2010). This LLJ formation mechanism is very similar to that over some other coastal regions, including the Baltic Sea (Smedman et al., 1995; Tjernström & Smedman, 1993), and the eastern coast in the US (Helmis et al., 2013; Mahrt et al., 2014), where offshore winds lead to advection of relatively warm air over generally colder sea surface. Frictional decoupling due to the strong stability induces the LLJ, producing an analogy to the well-known nocturnal boundary layer jet elucidated by Blackadar (1957).

To further confirm the role of near-surface stability and vertical mixing in the development of these LLJs, WRF sensitivity simulations with YSU are conducted in which the stability dependence of the eddy diffusivity is systematically varied. In YSU, the velocity scale used to calculate eddy diffusivity is inversely proportional to a non-dimensional profile function, ϕ_m. For the stable boundary layer ($z/L > 0$) in YSU ϕ_m is implemented as

$$\phi_m = 1 + \alpha \frac{z}{L}, \tag{3}$$

where L is the Monin-Obukhov length. The coefficient α, which describes the dependence of eddy diffusivity on the stability parameter z/L, plays an important role for simulating LLJs. Its default value in YSU is 5 (Hu et al., 2013; Nielsen-Gammon et al., 2010). Sensitivity simulations with a varying between 0.01 and 5 are conducted following the approach proposed by Klein et al. (2016) to modulate stable boundary layer mixing and to minimize the impact on convective boundary layer and other large scale dynamics. These sensitivity simulations are meticulously designed to illustrate the impact of near-surface vertical mixing on LLJ development. Decreasing α in the YSU PBL scheme causes stronger vertical mixing in the stable boundary layer, leading to weaker LLJs at the top of the stable boundary layer (Figure 10). Thus, these sensitivity simulations illustrate the relationship between near-surface vertical mixing strength and LLJ strength, and thus prove that these shallow marine LLJs develop due to weakened near-surface mixing and increased stability as a result of warm advection, corroborating previous studies (Mahrt et al., 2014). Synoptic scale wind shears, which trigger upper layer jets as shown in other studies (Truong et al., 2023), may only play a secondary role in the development of the shallow LLJs lower than 950 hPa in the case shown in Figure 9.

Above the shallow stable boundary layer, there was a decoupled/separated cloud layer at about 1.4–2 km as indicated by the 100% RH (Figure 9) and radar reflectivity of ~–35 dBZ at 18 UTC (Figure 11). All the four PBL schemes reproduce such a decoupled cloud-boundary layer, including the shallow boundary layer with an LLJ at its top and the decoupled cloud layer above 1.4 km (Figure 9). The difference between the PBL schemes is small (Figure 9) due to similar eddy diffusivity in the stable boundary layer (Hu et al., 2013). Note that from 12 to 18 UTC on January 10, the Aurora Australis traveled from 46°S to 45.07°S and the cloud-boundary layer coupling

10.1029/2025JD043679

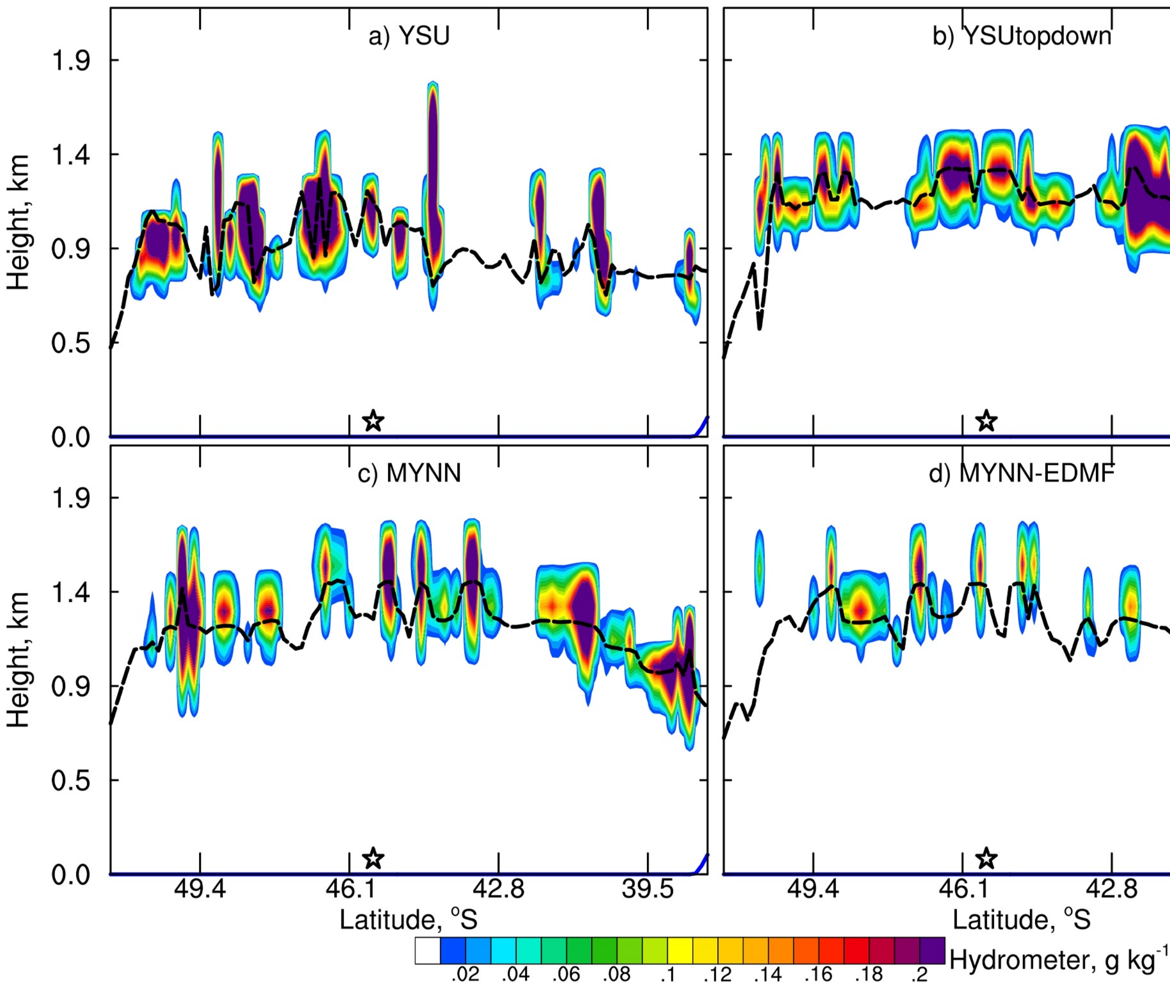

Figure 7. South-north cross-sections of cloud hydrometer in a coupled cloud-boundary layer at 12 UTC on 1 December 2017 simulated by WRF with four PBL schemes, (a) YSU, (b) YSUtopdown, (c) MYNN, (d) MYNN-EDMF. The star on *x*-Axis marks the location of supply vessel Aurora Australis (45.47°S, 142.3°E). Simulated PBL top is marked by a dashed line.

transitioned from a coupled mode to a decoupled mode (Figure 11). Around 12 UTC, clouds developed across the boundary layer top at ∼0.9 km over the region around 46°S as shown in the simulated cross-sections. YSU-topdown simulates a deeper boundary layer than YSU by ∼100 m in this region similar to the case explained in Section 3.2. When the Aurora Australis traveled northward from 46°S to 45.07°S during 12–18 UTC, warm advection associated with northerly winds leads to development of a shallow stable boundary layer and a decoupled cloud layer at 1.4–1.9 km as indicated by the simulations and radar reflectivity. All four PBL schemes generally reproduce the vertical cloud distribution during the transition from the coupled to decoupled cloud-boundary layer from 46°S to 45.07°S during 12–18 UTC (Figure 11).

3.4. Decoupled Cloud-Boundary Layer in the Presence of Strong Positive H_s, With Deeper Surface-Based PBL

3.4.1. Analysis Using Observational Data and Simulations With Four PBL Schemes

On 18 February 2018, when the NSF/NCAR GV flew back over the Southern Ocean to Australia, a cyclone to the south of Australia moved eastward. On the western side of the cyclone, an anticyclone developed over the ocean to the southwest of Tasmania, Australia. Thus, southwesterly winds (that led to cold air advection) between the cyclone and anticyclone prevailed over the ocean to the south of Tasmania (Figures 4 and 12, refer to Truong et al. (2020) for detailed synoptic conditions of this case). The tongue of cold air south of Tasmania appears as cumuliform clouds (see the Himawari-8 visible image at 7 UTC in Figure 1 and LWP in Figure 12h), which was

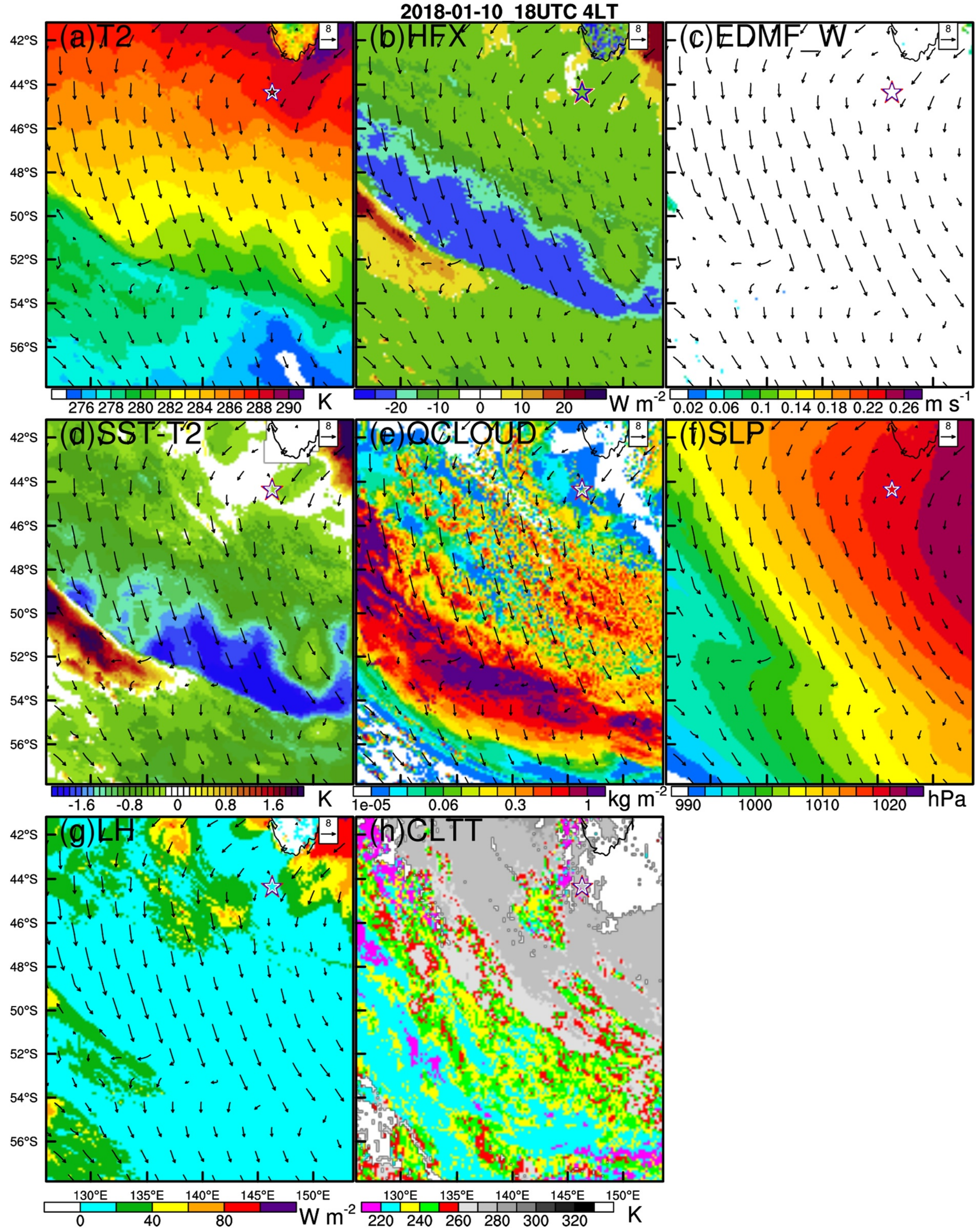

Figure 8. Spatial distribution of simulated (a) T2, (b) sensible heat flux (HFX), (c) mass flux vertical velocity (EDMF_W) at the first layer, (d) SST-T2, (e) integrated cloud water, (f) sea level pressure (SLP), (g) latent heat flux (LH), and (h) cloud top temperature (CLTT) from the Himawari satellite at 18 UTC on 10 January 2018. The location of the Aurora sounding is marked by a star.

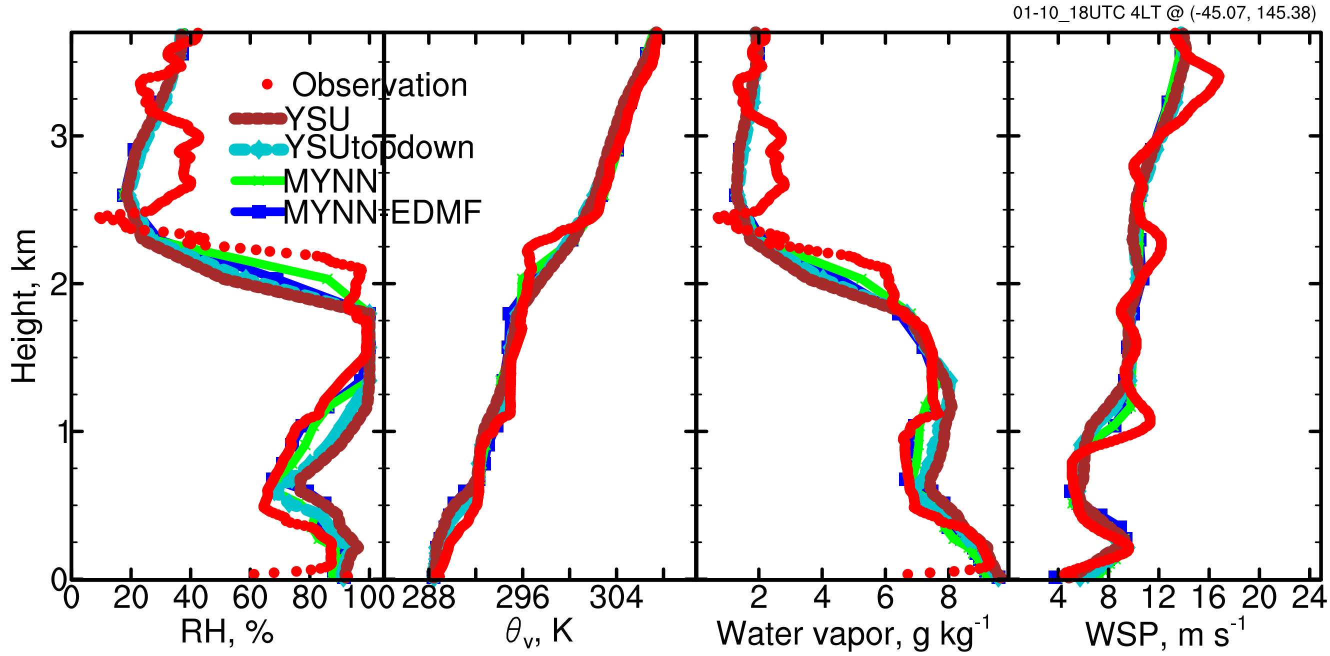

Figure 9. Profiles of (left to right) RH, virtual potential temperature (θ_v), Water vapor mixing ratio, and wind speed in a decoupled cloud-boundary layer at 18 UTC on 10 January 2018 observed by Aurora sounding and simulated by WRF with four PBL schemes.

sampled by the dropsonde from the GV at 7 UTC (Figure 13). The CALIPSO backscatter coefficient measured at 3 hr earlier (4 UTC) also indicates scattered cumuliform clouds with cloud tops at 1.8–2.5 km between 45 and 50°S (Figure 14e). Such clouds often develop in the cold tongues of mesoscale cyclones over the Southern Ocean (Papritz et al., 2015). In the presence of cold advection over the warmer ocean, there was strong surface latent flux (>80 W m^{-2}, Figure 12g) and sensible heat flux (>40 W m^{-2}, Figure 12b), which produced a deeper surface-based PBL (>1 km). All the PBL schemes simulate a thick PBL (Figure 13) and scattered clouds (Figures 12, 14 and 15). Compared to the Himawari observation, WRF simulations reproduce the spatial distribution of LWP with lower LWP in the cold tongue. The WRF simulation shows an underestimation of cloud cover. Such an underestimation appears to be a common issue of many NWP and climate models when simulating stratiform

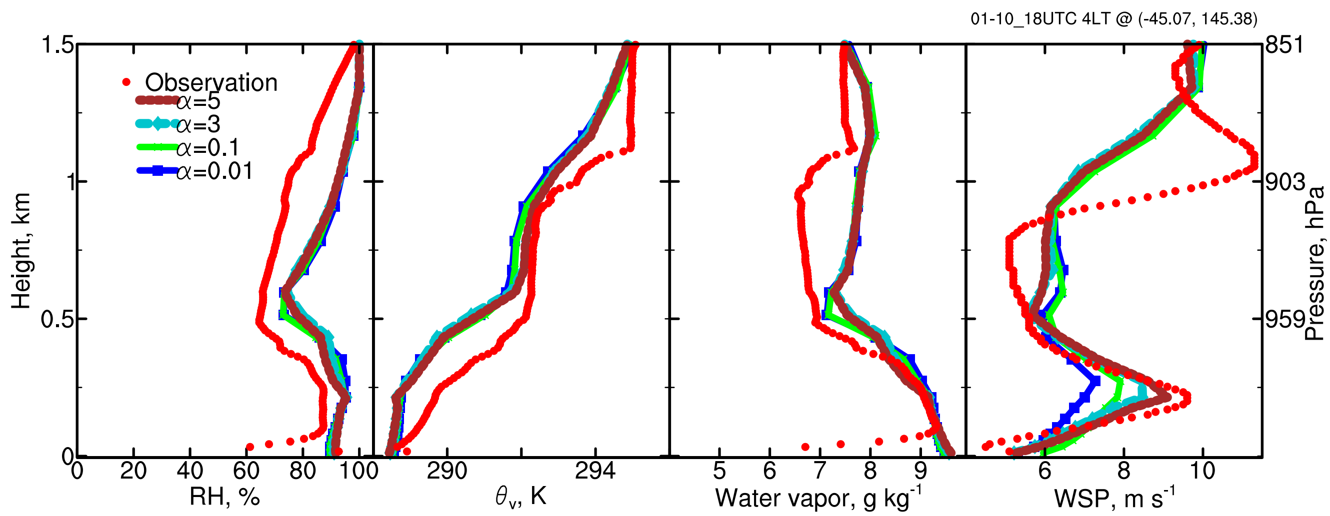

Figure 10. Profiles of (left to right) RH, virtual potential temperature (θ_v), Water vapor mixing ratio, and wind speed in a decoupled cloud-boundary layer at 18 UTC on 10 January 2018 observed by the Aurora Australis sounding and simulated by WRF with the YSU PBL schemes with different α values.

10.1029/2025JD043679

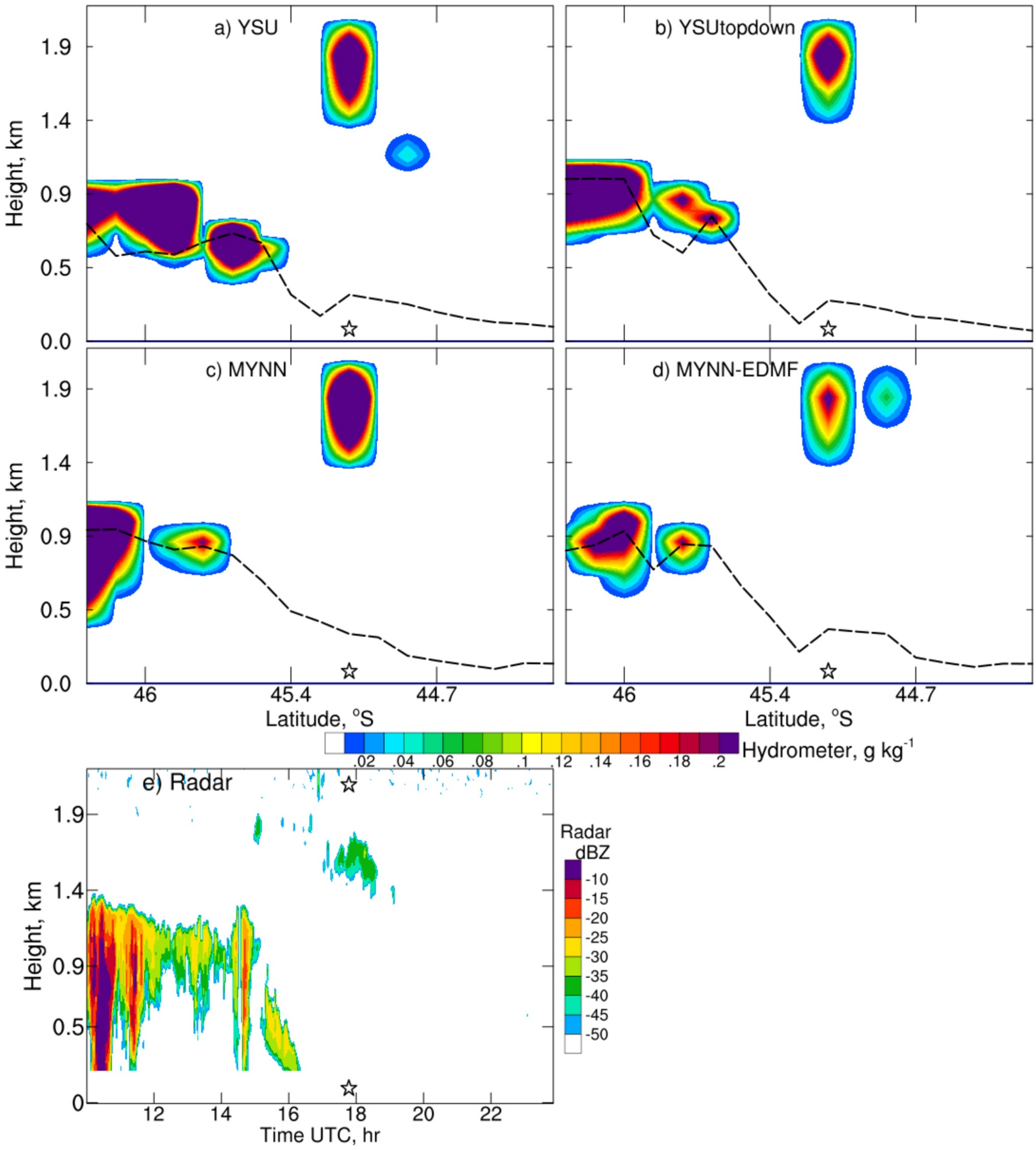

Figure 11. South-north cross-sections of cloud hydrometer following track of supply vessel Aurora Australis on 10 January 2018 simulated by WRF with four PBL schemes, (a) YSU, (b) YSUtopdown, (c) MYNN, (d) MYNN-EDMF, (e) reflectivity from the W-band (95 GHz) cloud radar deployed on Aurora. The star on *x*-Axis marks the location of supply vessel Aurora Australis (45.07°S, 145.38°E) at 17:47 UTC when the sounding of Figure 9 was launched. Simulated PBL top is marked by a dashed line. Note that the simulation is extracted from the hourly outputs to match the radar time.

clouds in the presence of cold advection, which is related to uncertainties in model treatments such as microphysics schemes (Duynkerke & Teixeira, 2001; Field et al., 2014; Jakob, 1999; Liu et al., 2011; Morrison & Pinto, 2006).

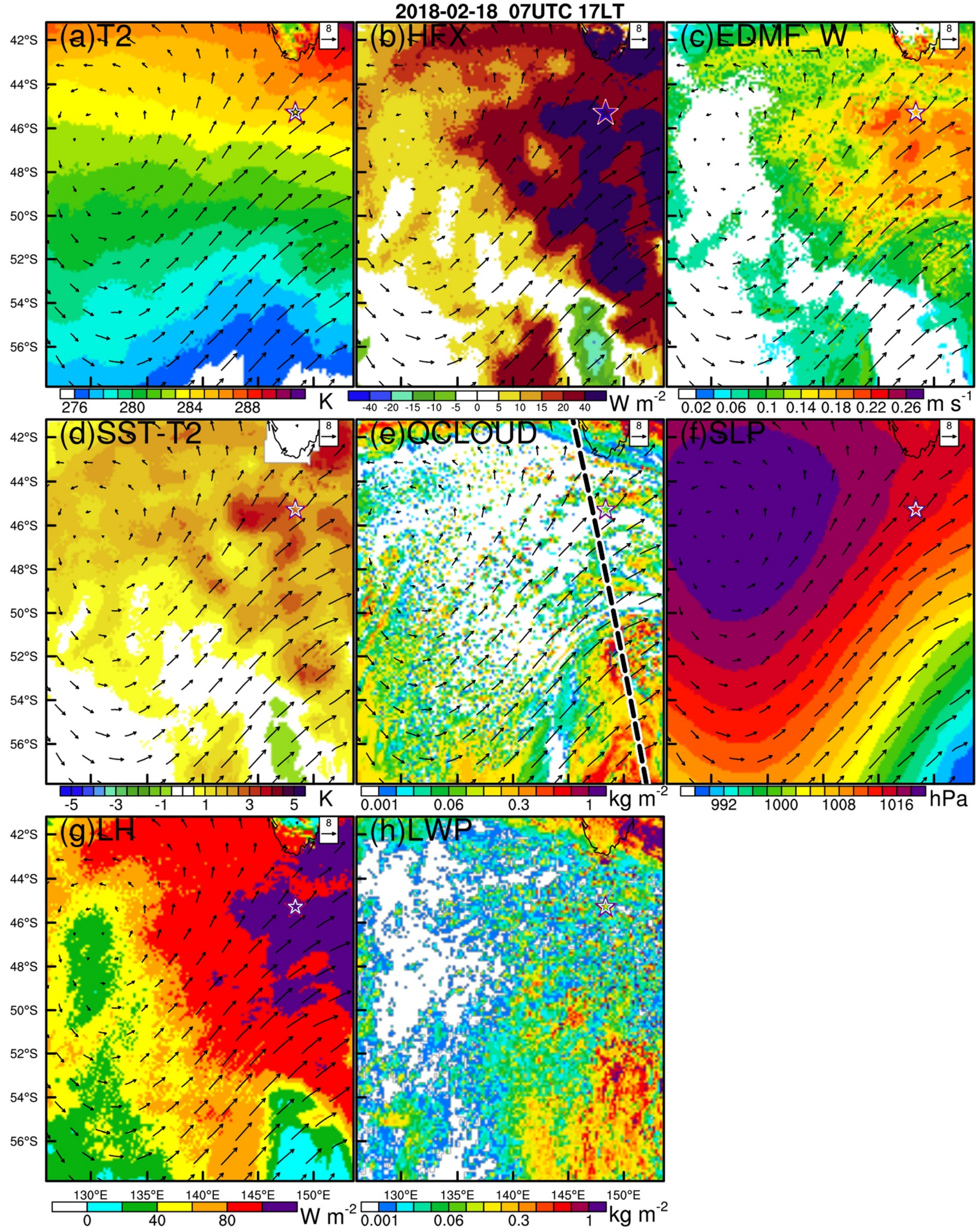

Figure 12. Spatial distribution of simulated (a) T2, (b) sensible heat flux (HFX), (c) mass flux vertical velocity (EDMF_W) at the first layer, (d) SST-T2, (e) integrated cloud water, (f) sea level pressure (SLP), (g) latent heat flux (LH), and (h) cloud liquid water path (LWP) from the Himawari satellite at 7 UTC on 18 February 2018. The location of the NSF/NCAR GV dropsonde is marked by a star. The track of CALIPSO at 4 UTC is marked in panel (e).

10.1029/2025JD043679

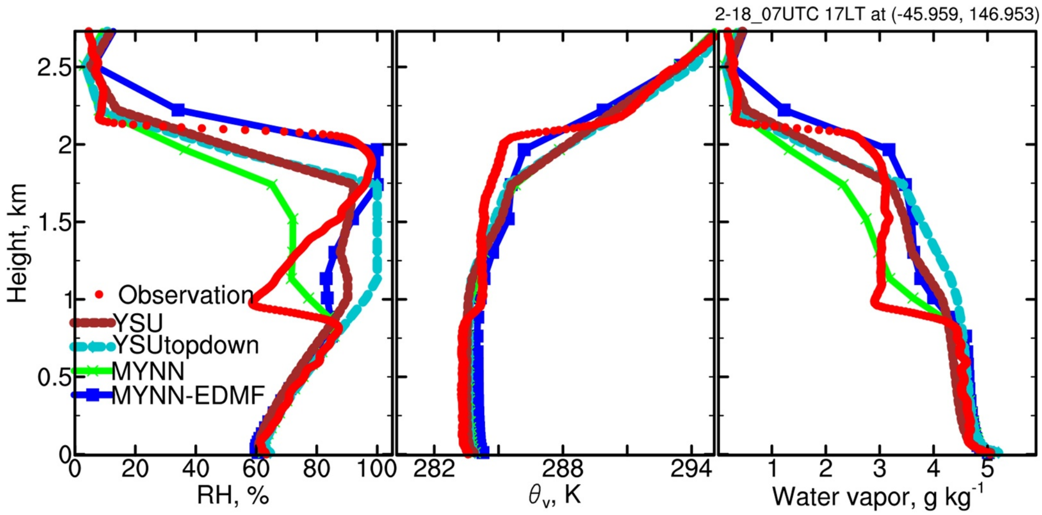

Figure 13. Profiles of (left to right) RH, virtual potential temperature (θ_v), Water vapor mixing ratio in a decoupled cloud-boundary layer at 07 UTC on 18 February 2018 observed by GV dropsonde (45.959^{o}S, 146.953^{o}E) and simulated by WRF with four PBL schemes.

This study focuses on the impact of uncertainties in PBL schemes on the cloud-boundary layer coupling mode. While YSU and MYNN simulate a coupled cloud-boundary layer, MYNN-EDMF simulates a decoupled cloud-boundary layer between 50.2 and 44.8°S, a region as wide as 500 km in south-north direction at both 4 UTC (CALIPSO track time, Figure 14) and 7 UTC (GV dropsonde time, Figures 13 and 15). A cloud layer is maintained above the PBL and is clearly separated from the PBL in the MYNN-EDMF simulation, while the cloud layer is maintained across the PBL top in the simulations with other PBL schemes (Figure 15). The cloud top simulated by MYNN-EDMF at 4 UTC appears consistent with the CALIPSO backscatter cross-section that indicates cloud tops at 1.8–2.5 km (Figure 14). The decoupled cloud-boundary layer simulated with the MYNN-EDMF shows the best agreement with the NSF/NCAR GV dropsonde data, which shows a two-layer structure, with a surface-based PBL up to ∼1 km, and an overlaying mixed layer topped at ∼2 km, above which the RH reaches ∼100% indicating the presence of clouds (Figure 13). Note that there is horizontal variability in the soundings, however, the cloud-boundary layer coupling status is not affected by the horizontal variability as shown in hydrometer cross-sections (Figures 14 and 15). Cross-sections for RH and potential temperature are also examined. The horizontal variability of RH closely follows that of hydrometers with intermittent high RH due to scattered cloud formation. The cross-section of RH further illustrates that the cloud layer (area with RH > 95%) is clearly separated from the boundary layer top in the MYNBN-DEMF simulation (Figure 16), which shows the best agreement with the GV dropsonde (Figure 13). The horizontal variability of potential temperature (Figure 17) appears less intermittent than RH and hydrometers likely due to the mixing process.

Conventional PBL schemes, such as the YSU and the MYNN, transport surface moisture to the PBL top where the temperature is low, and clouds develop near the PBL top. Above the PBL, since vertical mixing is weak in the free troposphere in conventional PBL schemes (Hu et al., 2012), moisture is hard to be transported further upward, and clouds are unlikely to develop above. Thus, clouds simulated by these conventional PBL schemes stay near the PBL top. In contrast, the MYNN-EDMF scheme adds a mass flux (MF) component for the representation of nonlocal updrafts from the surface up to the cloud layer, in addition to the MYNN eddy-diffusivity (ED) local mixing closure. The local mixing within the surface-based PBL and the mass flux nonlocal mixing may have different vertical extents (Olson, Kenyon, Angevine, et al., 2019; Olson, Kenyon, Djalalova, et al., 2019; Pergaud et al., 2009). Thus, while MYNN-EDMF simulates a surface-based PBL with a depth of 1 km, in the presence of strong surface positive flux the nonlocal mass flux develops in the region (as indicated by the spatial distribution of mass flux vertical velocity at the first layer in Figure 12), and the convective updrafts penetrates 2 km above the surface (as indicated by the profile of updraft velocity in Figure 18). As a result, the nonlocal flux is able to deposit moisture at 2 km where a cloud layer develops that is decoupled from the 1 km-deep PBL below in a region as wide as 500 km in the south-north direction (Figure 15). Thus, the MYNN-EDMF scheme captures the 2-layer

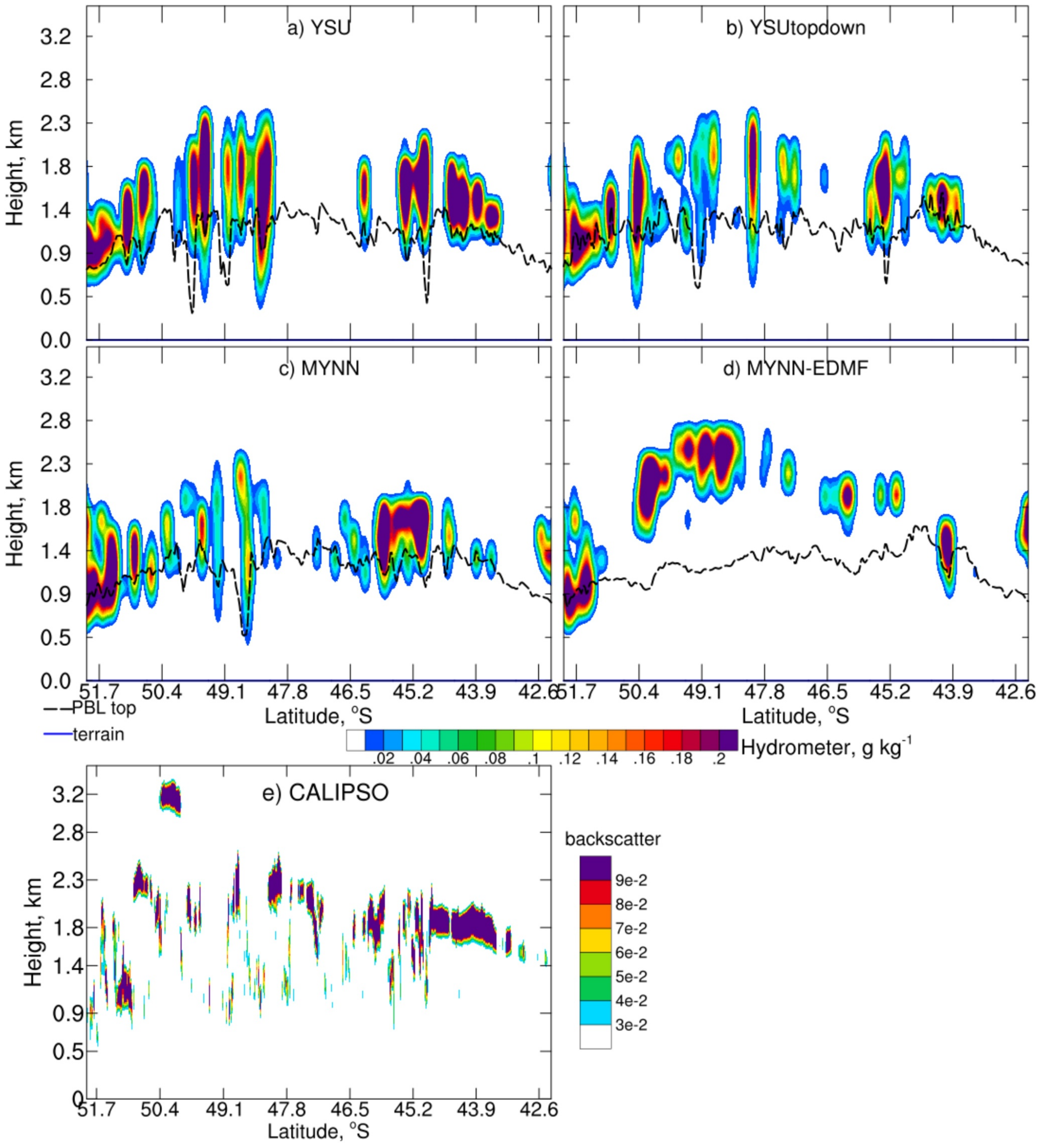

Figure 14. Cross-sections of cloud hydrometers along the CALIPSO track shown in Figure 12e at 04 UTC on 18 February 2018 simulated by WRF with four PBL schemes, (a) YSU, (b) YSUtopdown, (c) MYNN, (d) MYNN-EDMF. (e) backscattering coefficient at 532 nm from CALIPSO. Simulated PBL top is marked by a dashed line.

PBL structure as indicated by potential temperature and water vapor mixing ratio better than other conventional PBL schemes. The latter simulate larger gradients of potential temperature and moisture above the surface-based PBL because they have weaker mixing in the free troposphere (Figure 13).

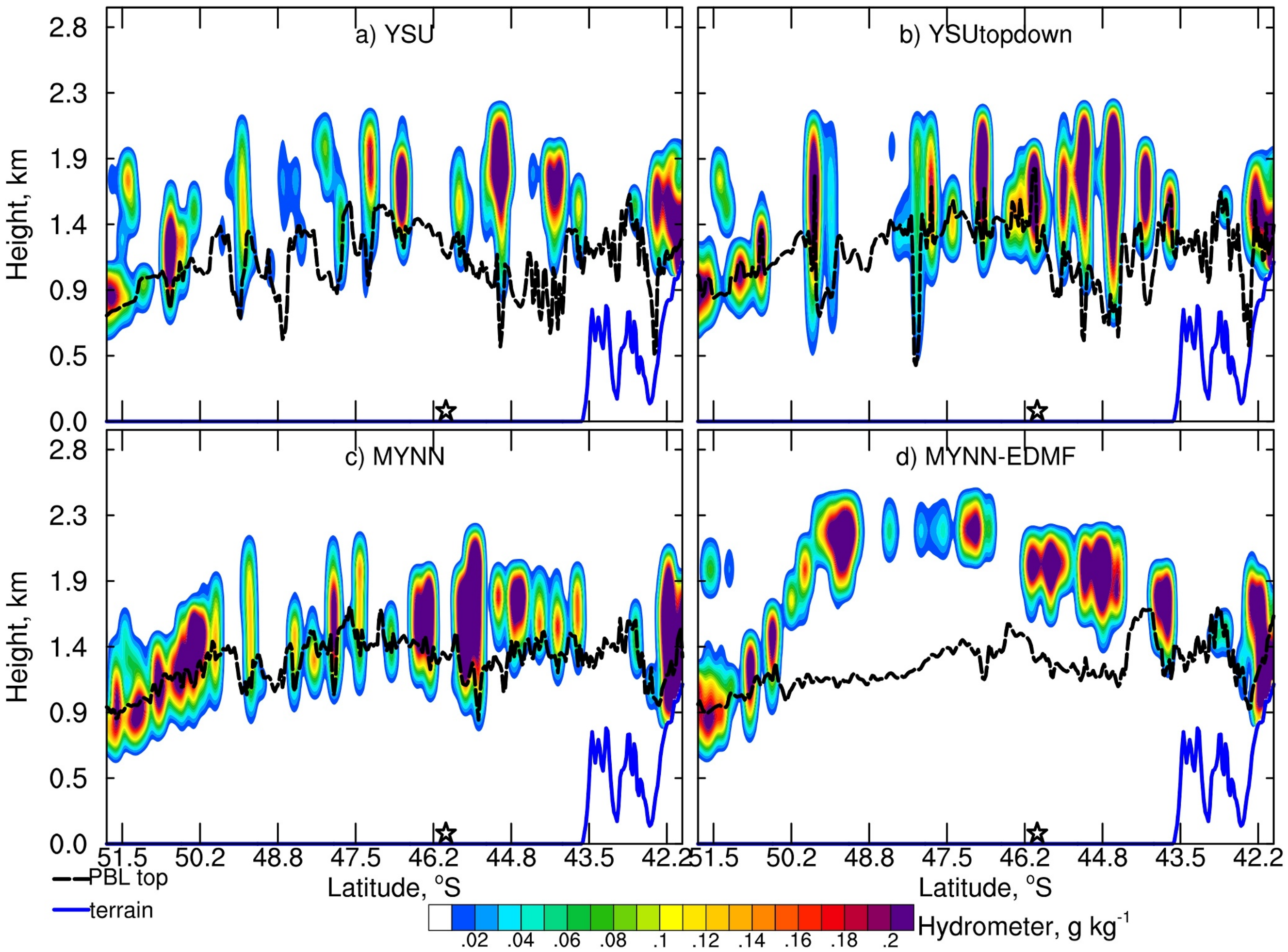

Figure 15. South-north cross-sections of cloud hydrometer at 07 UTC on 18 February 2018 simulated by WRF with four PBL schemes, (a) YSU, (b) YSUtopdown, (c) MYNN, (d) MYNN-EDMF. The location of the NSF/NCAR GV dropsonde (45.959°S, 146.953°E) is marked by a star on *x*-Axis. Simulated PBL top is marked by a dashed line.

3.4.2. Sensitivity Experiments With the MYNN-EDMF Scheme

The primary difference between MYNN-EDMF and other convectional PBL schemes is that MYNN-EDMF has an additional mass flux nonlocal mixing treatment, which plays a critical role in reproducing the decoupled cloud-boundary layer in the presence of strong surface sensible heat fluxes. Such a conclusion is clearly proven by the different performance between MYNN-EDMF (simulating decoupled cloud-boundary layer) and MYNN (simulating coupled cloud-boundary layer), because the only difference between these two experiments is the mass flux treatment and thus its effect is isolated. The effect is most apparent over 50.2–44.8°S, a region as wide as 500 km.

To further understand the behavior of the mass flux treatment of MYNN-EDMF, additional parameter sensitivity experiments are conducted by varying two selected empirical parameters, the empirical capping height of individual plumes (h_p), and the empirical coefficient for the fractional entrainment rate of individual plumes (c_ε). By limiting h_p to 500 m, moisture above the PBL quickly decreases and the model underestimates moisture at 2 km above the surface where clouds develop in the observations (Figure 19). As a result, clouds above the PBL disappear and instead the cloud layer develops across the boundary layer top over 50.2–44.8°S, similar as in other conventional PBL schemes (Figure 20a). When setting h_p to 2,500 m or 4,500 m, more moisture is deposited at 2 km above the surface where a separate cloud layer develops that is decoupled from the PBL below (Figures 20b

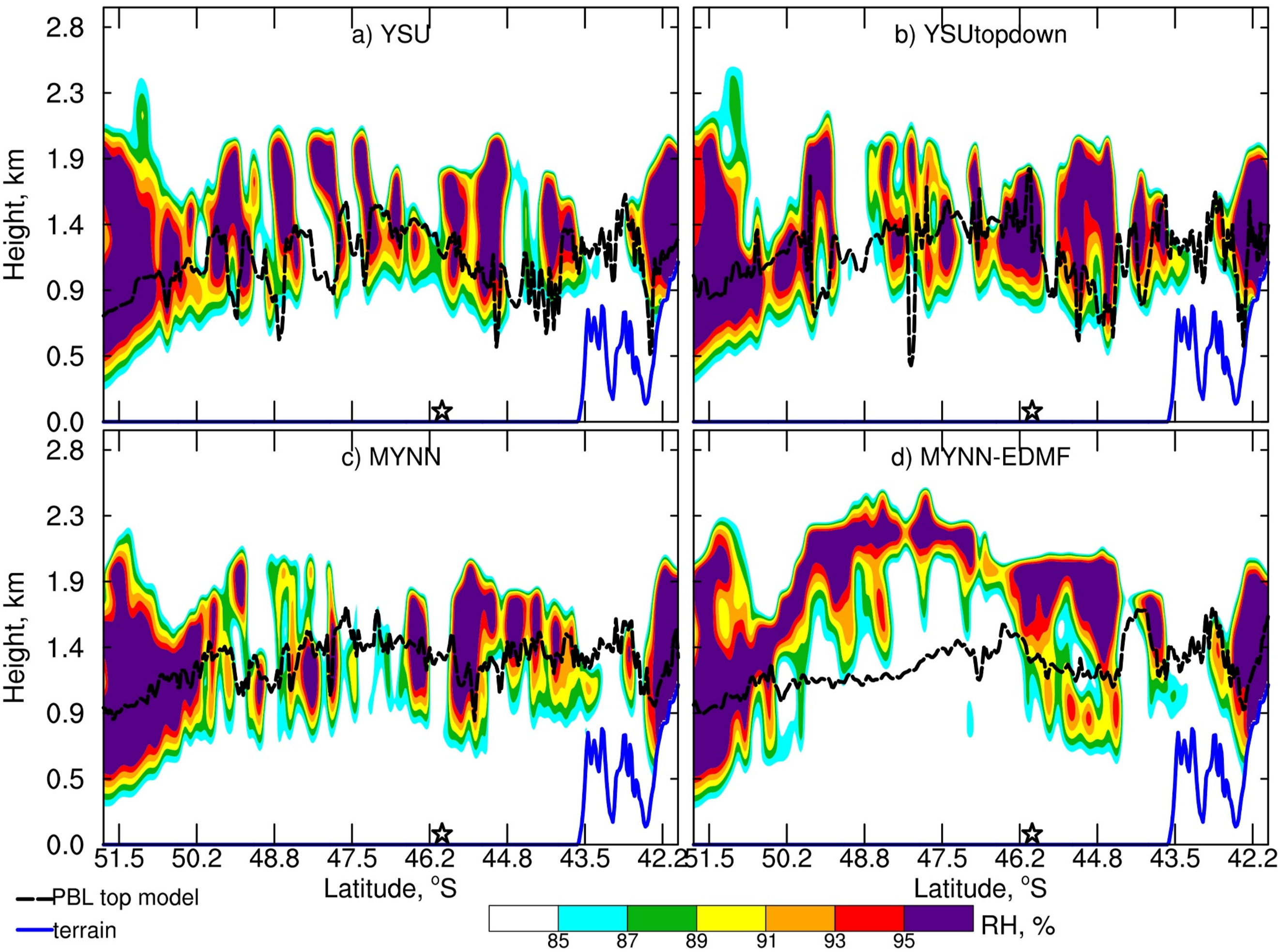

Figure 16. Same as Figure 15, but for relative humidity (RH).

and 20c), similar to the default MYNN-EDMF in WRF with h_p of 3,500 m (Figure 15d). Thus, h_p plays a critical role in the vertical transport of moisture and deposits moisture in either within PBL or above PBL.

Entrainment rate also plays a critical role in simulating the type 3 decoupled mode. With c_ε set to 0.2 m s^{-1}, the decoupled cloud-boundary layer is simulated over 50.2–44.8°S (Figure 20d), similar as the default MYNN-EDMF with c_ε set to 0.33 m s^{-1}. When c_ε is increased to 0.55 or 0.9 m s^{-1}, WRF appears to underestimate the upward transport of moisture to 2 km and underestimate the moisture deposit at 2 km, thus a separated cloud layer is not able to develop at 2 km. Instead clouds only develop across the boundary layer top and thus a coupled cloud-boundary layer is simulated over 50.2–44.8°S as in the conventional PBL schemes (Figures 20e and 20f). It appears c_ε is highly related to the updraft penetration depths. With larger c_ε (>0.55 m s^{-1}), plumes cannot penetrate as deep as suggested by the observations, likely because strong entrainment already dissipates the plume energy before the plumes are able to penetrate as high as 2 km. The parameter of c_ε is essentially an assessment of the strength of turbulent kinetic energy (TKE). Since shallow cumulus generally does not have a large turbulent strength, such a large of c_ε (0.9) may not be physical. Nevertheless, these sensitivity simulations with h_p and c_ε further confirm that the advantage of the MYNN-EDMF scheme over other convectional PBL schemes to reproduce the decoupled cloud-boundary layer in the presence of strong surface positive flux is due to its mass-flux treatment.

4. Conclusions and Discussion

The boundary layer structure, particularly in terms of the coupling mode between the boundary layer and cloud layer, over the Southern Ocean is examined using WRF simulations, sounding data collected during three field

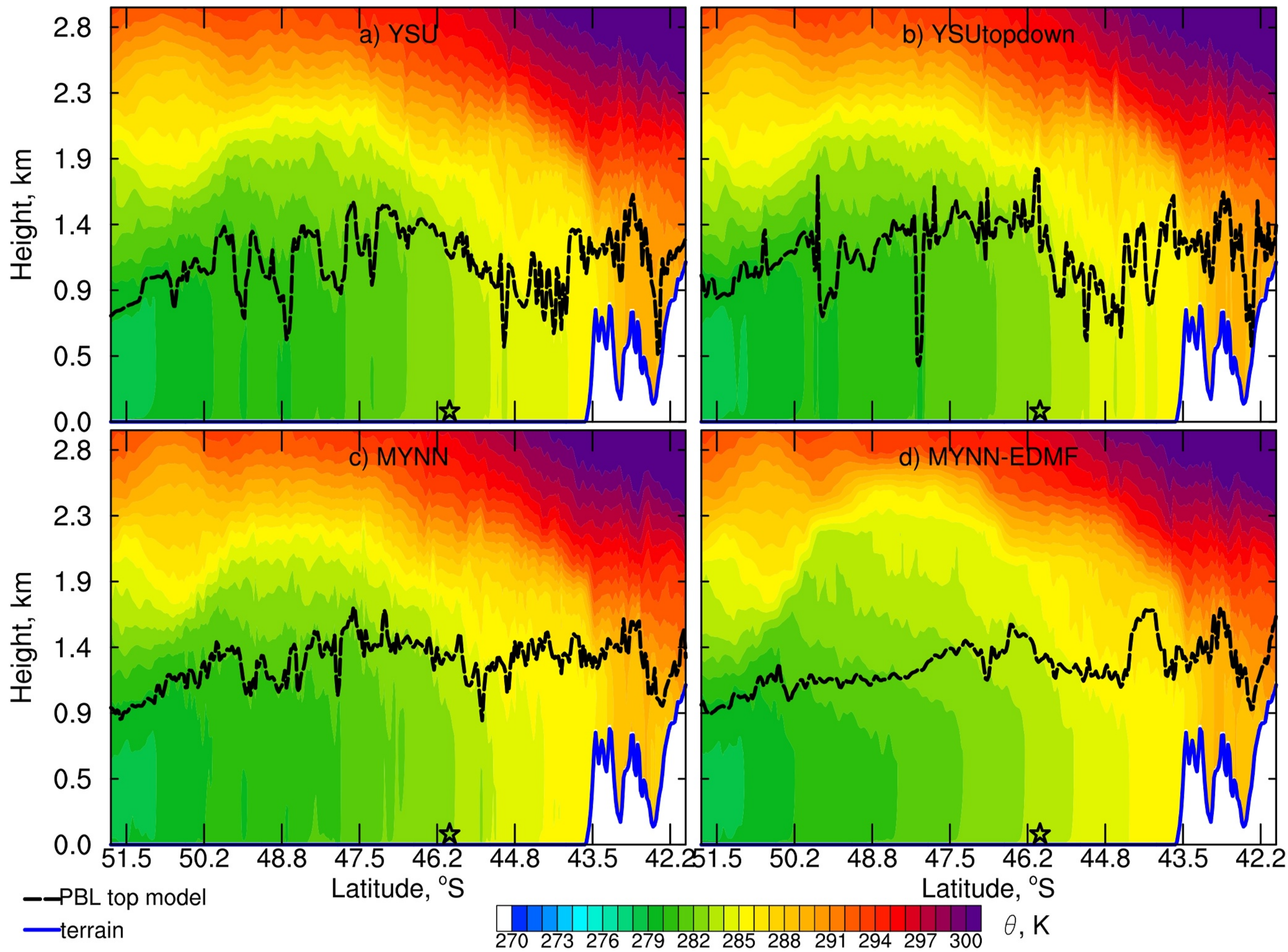

Figure 17. Same as Figure 15, but for potential temperature (θ).

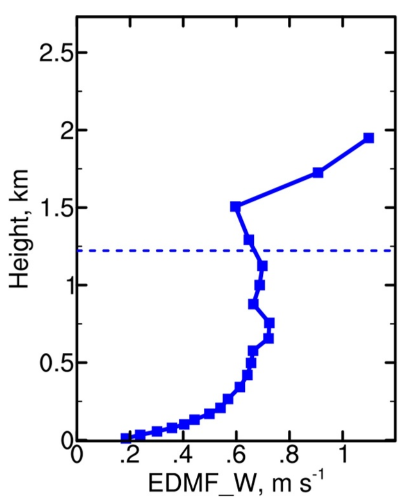

Figure 18. Profiles of mass flux vertical velocity (EDMF_W) at 07 UTC on 18 February 2018 at a GV dropsonde location simulated by WRF with the MYNN-EDMF PBL scheme. Simulated PBL top is marked by a dashed line.

experiments, and satellite observations. Nine single cloud layer cases over Southern Ocean with similar characteristics, including 1 December 2017, 21–22 March 2018, 23 March 2018, 10 January 2018 detected during the MARCUS experiment, and 17–18 February 2018 detected during the CAPRICORN and SOCRATES experiments, are simulated using the WRF model with three conventional and one mass-flux type PBL schemes. With the assistance of WRF simulations, the nine cases can be classified into three cloud-boundary layer coupling modes: 1. Coupled cloud-boundary layer in the presence of weak surface positive flux; 2. Decoupled cloud-boundary layer in the presence of surface negative flux, with a very shallow surface-based PBL; and 3. Decoupled cloud-boundary layer in the presence of single-layer high clouds and stronger surface positive flux, with thicker surface-based PBL. The major differences between Mode 1 and 3 are the magnitude of surface positive sensible heat flux and cloud layer height, with Mode 1 having a cloud layer at ~1 km, and Mode 3 having a cloud layer as high as 2 km that is above (decoupled from) the boundary layer top at ~1 km above the surface. The height difference between Mode 1 and 3 boundary layers and their transitions were discussed previously (Jones et al., 2011; Miller & Albrecht, 1995; Nicholls, 1984; Wood, 2012), but we provide a physically more intuitive classification in this study. Mode 1 represents a well-mixed cloud-topped PBL, common

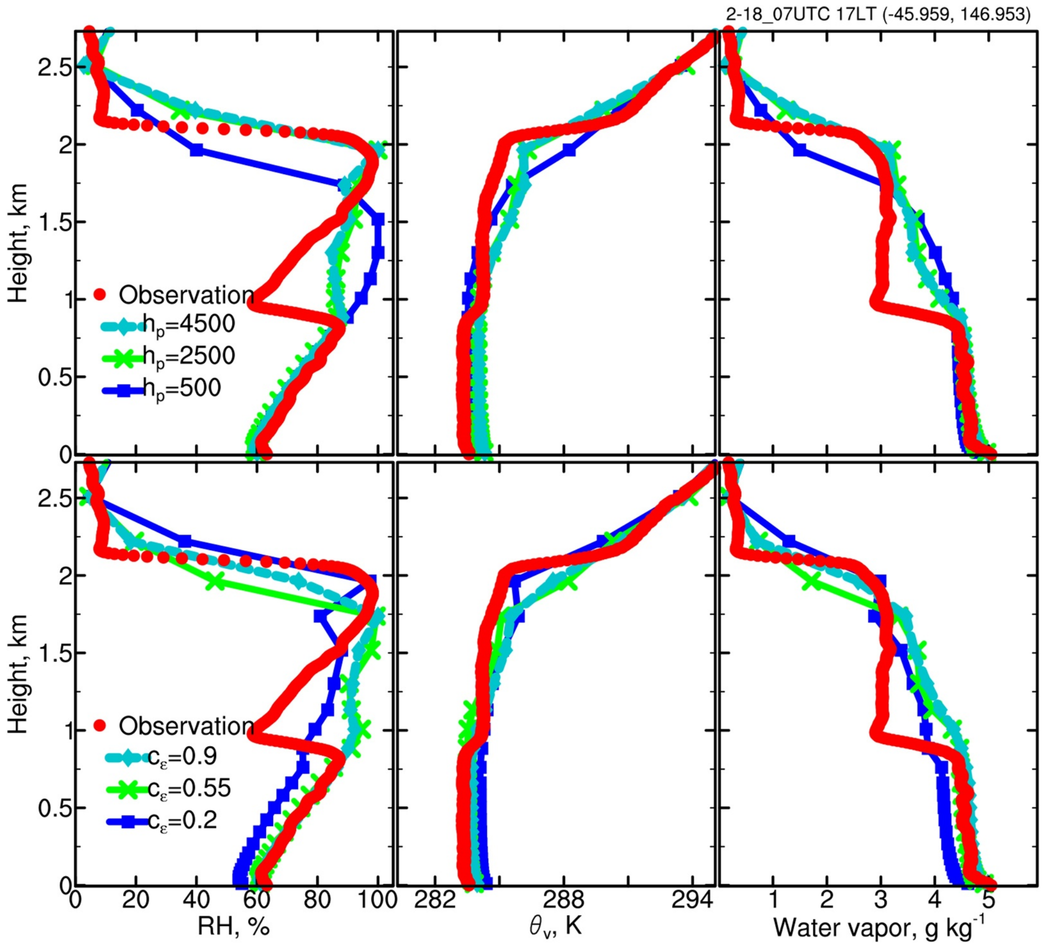

Figure 19. Profiles of (left to right) RH, virtual potential temperature (θ_v), Water vapor mixing ratio in a decoupled cloud-boundary layer at 07 UTC on 18 February 2018 observed by GV dropsonde (45.959°S, 146.953°E) and simulated by WRF with perturbed parameters (top) h_p = 500, 2,500, 4,500, (bottom) c_ε = 0.2, 0.55, 0.9 in MYNN-EDMF, see Table 1 for the model configuration.

over subtropical and midlatitude oceans with weak cold advection (Wood, 2012). These stratocumulus decks are climatically significant for Earth's radiative balance (Andrews et al., 2012; Hartmann et al., 1992; Qu et al., 2014). Mode 2 is a highly stratified PBL, frequently occurring under warm air advection over mid-latitude oceans. Previous studies (Zhang et al., 2023; Zheng & Li, 2019; Zheng, Zhang, Rosenfeld, et al., 2021) highlight the role of such decoupling in prolonging cloud lifetimes, which has implications for cloud feedbacks. Mode 3 is similar to the cumulus-topped boundary layer (Wood, 2012) and often occurs during subtropical stratocumulus-to-cumulus transitions driven by strong surface fluxes that deepen the PBL, a process referred to as the deepening-warming decoupling (Bretherton & Wyant, 1997; Sandu & Stevens, 2011; Wyant et al., 1997; Zheng et al., 2020). Accurately modeling this mode is crucial for improving simulations of stratocumulus-to-cumulus transitions, a persistent challenge in global climate models (Albrecht, 1993; Chung & Teixeira, 2012; Teixeira et al., 2011; Wang, 1993; Wang et al., 2015). Our cloud-boundary layer coupling classification, corroborating a similar classification proposed by Zheng et al. (2020), highlights the importance of cold/warm advection and the resulting positive/negative fluxes and near-surface stability on cloud-boundary layer coupling modes. These prerequisite conditions are related to shifts in winds and humidity that are induced by storm track at times (Hande et al., 2012). Comparing to the more extensively researched marine counterpart, continental stratocumuli occur less frequently (Mechem et al., 2010) and simulating stratocumulus-to-cumulus transitions over continents may be even more challenging due to the large magnitude and variability of surface fluxes (Ghonima et al., 2016; Hannak et al., 2017; Pedruzo-Bagazgoitia et al., 2020).

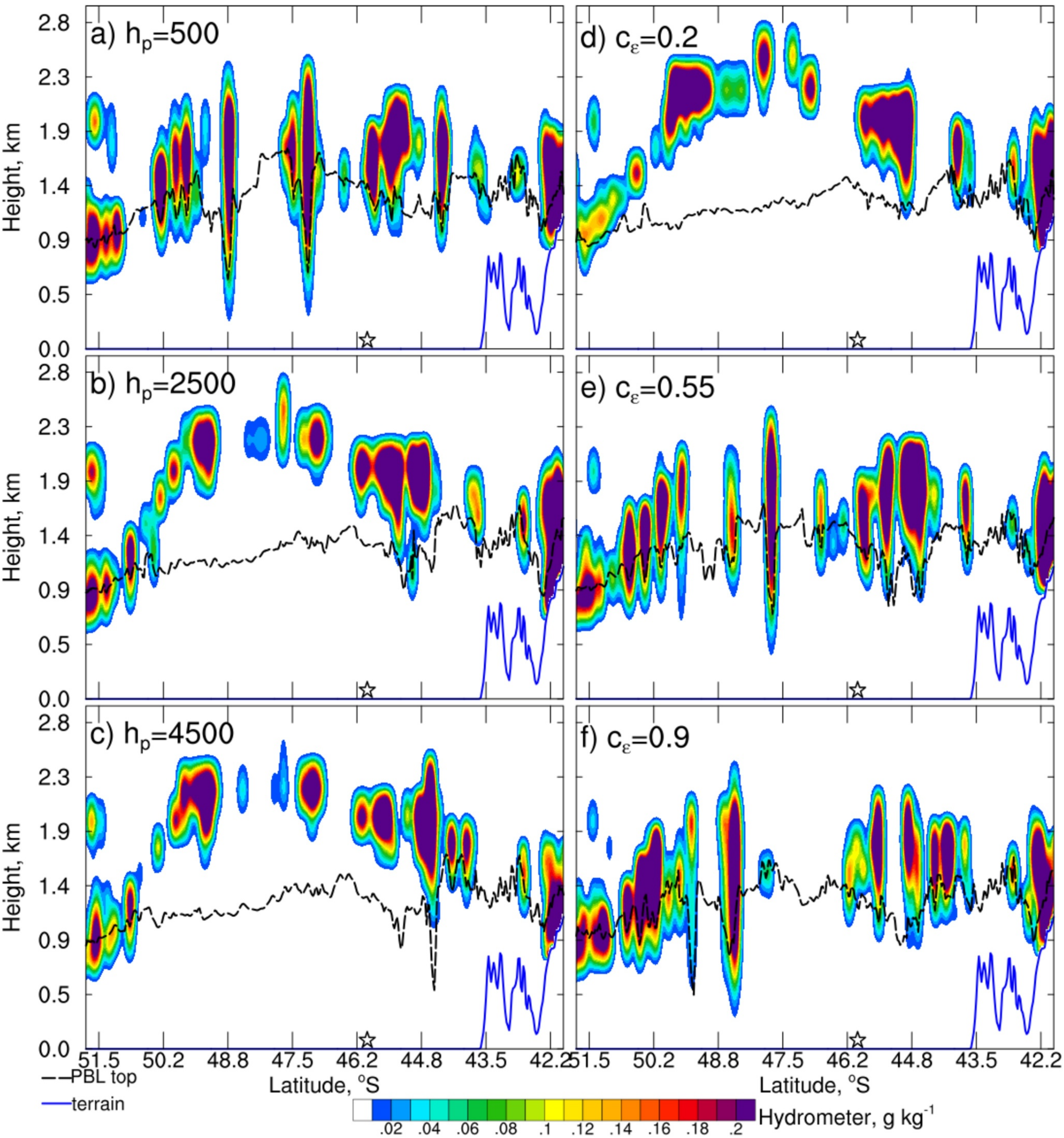

Figure 20. South-north cross-sections of cloud hydrometer at 07 UTC on 18 February 2018 simulated by WRF with perturbed parameters in MYNN-EDMF: (a) h_p = 500, (b) h_p = 2,500, (c) h_p = 4,500, (d) c_ε = 0.2, (e) c_ε = 0.55, (f) c_ε = 0.9, see Table 1 for the model configuration. The location of the NSF/NCAR GV dropsonde (45.959°S, 146.953°E) is marked by a star on x-Axis. Simulated PBL top is marked by a dashed line.

The performance of four PBL schemes, including three conventional schemes (YSU, YSUtopdown, and MYNN), and one mass flux type PBL scheme MYNN-EDMF is examined for three selected cases with one case representing one cloud-boundary layer coupling mode. For cases with the different cloud-boundary layer coupling modes, different PBL schemes provided the best consistency with observations. The YSUtopdown scheme has more consistency with observations than the YSU scheme for the type 1 coupling mode to simulate the higher cloud-topped boundary layer. With the additional top-down mixing from cloud-top radiative cooling considered, YSUtopdown simulates an enhanced entrainment process at the boundary layer top, which facilitates a deeper boundary layer growth, thus simulating higher boundary layer top clouds. The MYNN-EDMF scheme considering nonlocal mass flux in addition to a local eddy diffusivity treatment is more consistent with observations than the conventional PBL schemes for the type 3 coupling mode because of the different vertical extent of local mixing and nonlocal mass flux in presence of sufficient surface flux. In the presence of strong surface positive flux, the nonlocal mass flux penetrates through the boundary layer top. As a result, the nonlocal flux is able to deposit moisture in the free troposphere where a cloud layer develops that is decoupled from the PBL down below. Sensitivity simulations altering two parameters in the mass flux treatment in MYNN-EDMF are conducted, the empirical capping height of individual plumes (h_p), and the empirical coefficient for the fractional entrainment of individual plumes (c_ε). h_p and c_ε play an important role in simulating the cloud-boundary layer structure. Altering h_p and c_ε can lead to MYNN-EDMF simulating either coupled or decoupled cloud-boundary layers. These parameter sensitivity simulations further confirm that the advantage of the MYNN-EDMF scheme over other convectional PBL schemes in reproducing the decoupled cloud-boundary layer in the presence of strong surface positive flux is due to its mass-flux treatment. For the type 2 coupling mode, different PBL schemes perform similarly. These regional scale WRF simulations also essentially illustrate the impact of near-surface temperature gradients (i.e., the difference between SST and surface air temperature, either as a result of air advection or SST change) on the cloud-boundary layer coupling modes. These simulations corroborate previous idealized simulations applying a linear increasing/decreasing SST (Zheng, Zhang, & Li, 2021; Zheng, Zhang, Rosenfeld, et al., 2021), which proposed a similar cloud-boundary layer coupling classification as a function of air advection (Zheng et al., 2020).

The investigation of the three cloud-boundary layer coupling modes of this study is limited by the number of available soundings. For example, for the de-coupled mode on 18 February 2018, the model simulations suggest a de-coupled cloud layer above the boundary layer over 50.2–44.8°S, a region as wide as 500 km in the south-north direction, where there is only one sounding available from the dropsonde released from the NSF–NCAR GV aircraft. In addition, the dropsonde location is not at the center of the decoupled region where the decoupling characteristic is the most prominent (Figure 15d). In the prominent decoupling region, the cloud layer is higher than the PBL top by >1 km. More frequent soundings in the most representative regions can help investigate the development of these coupling modes and calibrate PBL schemes. Note that when using different PBL top diagnosing approaches, the resulting PBL height may differ by as much as 200–300 m (Hu et al., 2010; Liu & Liang, 2010). While most methods are primarily used for the continental PBL (Nielsen-Gammon et al., 2008), the Liu-Liang method uses different threshold parameters to diagnose PBL top over ocean and land (Liu & Liang, 2010). In addition to the PBL top diagnosed by PBL schemes, we also examined the PBL top diagnosed by the Liu-Liang method (Figure not shown). Over the ocean when the cloud layer is decoupled from the boundary layer, the PBL top diagnosed by the Liu-Liang method is ~200 m lower than the model-diagnosed PBL likely because the Liu-Liang method cut off the PBL height immediately into the inversion layer considering weaker convections over the ocean (Liu & Liang, 2010) while the model includes more of the inversion layer into the PBL. Over the continent the PBL heights diagnosed by the two are similar. Over the land-ocean interface and regions where the cloud layer and boundary layer are coupled, the PBL top diagnosed by the Liu-Liang method is oscillating. Diagnosing PBL height in such environments warrants future research attention. Nevertheless, our PBL mode classification method is physically more intuitive and superior to traditional stratification-based classifications (e.g., Jones et al., 2011) and the uncertainties associated with PBL-top diagnosing methods cannot change the coupling mode (with clouds developing cross PBL top) or decoupling mode (with the PBL top and cloud layer separated by as far as >1 km) discussed in this study.

This study examines the cloud-boundary layer coupling modes using simulations with a 3 km grid spacing. The choice of 3 km resolution is a trade-off between the need to include the widespread cloud system and limited computational resources. While the overall circulations of fully developed mesoscale cellular convections having the sizes of tens of kilometers can be resolved by the 3 km grid, the representation of detailed structures of the mesoscale cellular convection as well as its associated physical processes could certainly benefit from increased resolutions in future studies (Stevens et al., 2020).

Data Availability Statement

Sounding data (UCAR, 2024) were downloaded from NCAR's Earth Observing Laboratory, https://data.eol.ucar.edu/master_lists/generated/socrates/. The marine W-band (95 GHz) cloud Radar data (Lindenmaier et al., 2018) was downloaded from https://doi.org/10.5439/1973911. The Cloud-Aerosol Lidar and Infrared Pathfinder Satellite Observation (CALIPSO) satellite data (Winker et al., 2010) were downloaded from https://search.earthdata.nasa.gov/search/granules?p=C2445512043-LARC_ASDC. The Himawari data (NASA/LARC/SD/ASDC, 2018) were downloaded from https://doi.org/10.5067/HIM08/CERES/GEO_ED4_SH_V01.2. The ERA-Interim data used in this study were obtained from European Centre for Medium-Range Weather Forecasts (2009). Model data produced from this study (Hu, 2025) have been archived at CAPS website https://caps.ou.edu/micronet/SouthernOcean.html and the Luster NSF projects data server at the San Diego Supercomputer Center,/expanse/luster/projects/uok114/xhu2.

Acknowledgments

This work was primarily supported by DOE ASR projects (DE-SC0021159, DE-SC0025464) and by the National Science Foundation (NSF) through Grants AGS-1628674 and AGS-1762096. Ming Xue was also supported by NSF Grant AGS-1917701. The WRF simulations were performed on supercomputers Stampede 3 at the Texas Advanced Computing Center (TACC) through allocations TG-ATM160014 from the Advanced Cyberinfrastructure Coordination Ecosystem: Services & Support (ACCESS) program, which is supported by National Science Foundation Grants 2138259, 2138286, 2138307, 2137603, and 2138296. Some of the post-processing of simulations for this work was performed at the University of Oklahoma (OU) Supercomputing Center for Education and Research (OSCER). Discussion with Dr. Lan Gao helped interpret the satellite data. Three anonymous reviewers provided helpful comments that improved the manuscript.

References

Ahn, E., Huang, Y., Chubb, T. H., Baumgardner, D., Isaac, P., de Hoog, M., et al. (2017). In situ observations of wintertime low-altitude clouds over the Southern Ocean. *Quarterly Journal of the Royal Meteorological Society*, *143*(704), 1381–1394. https://doi.org/10.1002/qj.3011

Albrecht, B. A. (1993). Effects of precipitation on the thermodynamic structure of the trade wind boundary layer. *Journal of Geophysical Research*, *98*(D4), 7327–7337. https://doi.org/10.1029/93JD00027

Albrecht, B. A., Penc, R. S., & Schubert, W. H. (1985). An observational study of cloud-topped mixed layers. *Journal of the Atmospheric Sciences*, *42*(8), 800–822. https://doi.org/10.1175/1520-0469(1985)042<0800:Aosoct>2.0.Co;2

Andrews, T., Gregory, J. M., Webb, M. J., & Taylor, K. E. (2012). Forcing, feedbacks and climate sensitivity in CMIP5 coupled atmosphere-ocean climate models. *Geophysical Research Letters*, *39*(9). https://doi.org/10.1029/2012GL051607

Angevine, W. M. (2005). An integrated turbulence scheme for boundary layers with shallow cumulus applied to pollutant transport. *Journal of Applied Meteorology*, *44*(9), 1436–1452. https://doi.org/10.1175/JAM2284.1

Angevine, W. M., Eddington, L., Durkee, K., Fairall, C., Bianco, L., & Brioude, J. (2012). Meteorological model evaluation for CalNex 2010. *Monthly Weather Review*, *140*(12), 3885–3906. https://doi.org/10.1175/Mwr-D-12-00042.1

Angevine, W. M., Olson, J., Kenyon, J., Gustafson, W. I., Endo, S., Suselj, K., & Turner, D. D. (2018). Shallow Cumulus in WRF parameterizations evaluated against LASSO large-eddy simulations. *Monthly Weather Review*, *146*(12), 4303–4322. https://doi.org/10.1175/MWR-D-18-0115.1

Arya, P. S. (2001). *Introduction to micrometeorology*. Elsevier Science.

Banta, R. M., Pichugina, Y. L., & Brewer, W. A. (2006). Turbulent velocity-variance profiles in the stable boundary layer generated by a nocturnal low-level jet. *Journal of the Atmospheric Sciences*, *63*(11), 2700–2719. https://doi.org/10.1175/Jas3776.1

Bender, F. A.-M., Engström, A., Wood, R., & Charlson, R. J. (2017). Evaluation of hemispheric asymmetries in marine cloud radiative properties. *Journal of Climate*, *30*(11), 4131–4147. https://doi.org/10.1175/JCLI-D-16-0263.1

Berg, L. K., Liu, Y., Yang, B., Qian, Y., Krishnamurthy, R., Sheridan, L., & Olson, J. (2021). Time evolution and diurnal variability of the parametric sensitivity of turbine-height winds in the MYNN-EDMF parameterization. *Journal of Geophysical Research: Atmospheres*, *126*(11), e2020JD034000. https://doi.org/10.1029/2020JD034000

Blackadar, A. K. (1957). Boundary layer wind maxima and their significance for the growth of nocturnal inversions. *Bulletin of the American Meteorological Society*, *38*(5), 283–290. https://doi.org/10.1175/1520-0477-38.5.283

Bodas-Salcedo, A., Andrews, T., Karmalkar, A. V., & Ringer, M. A. (2016). Cloud liquid water path and radiative feedbacks over the Southern Ocean. *Geophysical Research Letters*, *43*(20), 10938–10946. https://doi.org/10.1002/2016GL070770

Bodas-Salcedo, A., Webb, M. J., Brooks, M. E., Ringer, M. A., Williams, K. D., Milton, S. F., & Wilson, D. R. (2008). Evaluating cloud systems in the Met Office global forecast model using simulated CloudSat radar reflectivities. *Journal of Geophysical Research*, *113*(D8). https://doi.org/10.1029/2007JD009620

Bodas-Salcedo, A., Williams, K. D., Field, P. R., & Lock, A. P. (2012). The surface downwelling solar radiation surplus over the southern ocean in the met office model: The role of midlatitude cyclone clouds. *Journal of Climate*, *25*(21), 7467–7486. https://doi.org/10.1175/JCLI-D-11-00702.1

Bodas-Salcedo, A., Williams, K. D., Ringer, M. A., Beau, I., Cole, J. N. S., Dufresne, J.-L., et al. (2014). Origins of the solar radiation biases over the Southern Ocean in CFMIP2 models. *Journal of Climate*, *27*(1), 41–56. https://doi.org/10.1175/JCLI-D-13-00169.1

Bretherton, C. S., & Wyant, M. C. (1997). Moisture transport, lower-tropospheric stability, and decoupling of cloud-topped boundary layers. *Journal of the Atmospheric Sciences*, *54*(1), 148–167. https://doi.org/10.1175/1520-0469(1997)054<0148:MTLTSA>2.0.CO;2

Bright, D. R., & Mullen, S. L. (2002). The sensitivity of the numerical simulation of the southwest monsoon boundary layer to the choice of PBL turbulence parameterization in MM5. *Weather and Forecasting*, *17*(1), 99–114. https://doi.org/10.1175/1520-0434(2002)017<0099:Tsotns>2.0.Co;2

Cheng, A., & Xu, K.-M. (2011). Improved low-cloud simulation from a multiscale modeling framework with a third-order turbulence closure in its cloud-resolving model component. *Journal of Geophysical Research*, *116*(D14), D14101. https://doi.org/10.1029/2010JD015362

Ching, J. K. S. (1981). The role of convective clouds in venting ozone from the mixed layer. *Bulletin of the American Meteorological Society*, *62*(7), 1089.

Chung, D., & Teixeira, J. (2012). A simple model for stratocumulus to shallow cumulus cloud transitions. *Journal of Climate*, *25*(7), 2547–2554. https://doi.org/10.1175/JCLI-D-11-00105.1

Clark, A. J., Coniglio, M. C., Coffer, B. E., Thompson, G., Xue, M., & Kong, F. Y. (2015). Sensitivity of 24-h forecast dryline position and structure to boundary layer parameterizations in convection-allowing WRF model simulations. *Weather and Forecasting*, *30*(3), 613–638. https://doi.org/10.1175/Waf-D-14-00078.1

Cohen, A. E., Cavallo, S. M., Coniglio, M. C., & Brooks, H. E. (2015). A review of planetary boundary layer parameterization schemes and their sensitivity in simulating southeastern US cold season severe weather environments. *Weather and Forecasting*, *30*(3), 591–612. https://doi.org/10.1175/Waf-D-14-00105.1

Coniglio, M. C., Correia, J., Marsh, P. T., & Kong, F. Y. (2013). Verification of convection-allowing WRF model forecasts of the planetary boundary layer using sounding observations. *Weather and Forecasting*, *28*(3), 842–862. https://doi.org/10.1175/Waf-D-12-00103.1

Cotton, W. R., Alexander, G. D., Hertenstein, R., Walko, R. L., McAnelly, R. L., & Nicholls, M. (1995). Cloud venting—A review and some new global annual estimates. *Earth-Science Reviews*, *39*(3), 169–206. https://doi.org/10.1016/0012-8252(95)00007-0

Deardorff, J. W. (1966). Counter-gradient heat flux in lower atmosphere and in laboratory. *Journal of the Atmospheric Sciences*, *23*(5), 503–506. https://doi.org/10.1175/1520-0469(1966)023<0503:Tcghfi>2.0.Co;2

Deardorff, J. W. (1972). Theoretical expression for the countergradient vertical heat flux. *Journal of Geophysical Research*, *77*(30), 5900–5904. https://doi.org/10.1029/JC077i030p05900

Deardorff, J. W. (1980). Cloud top entrainment instability. *Journal of the Atmospheric Sciences*, *37*(1), 131–147. https://doi.org/10.1175/1520-0469(1980)037<0131:Ctei>2.0.Co;2

Dee, D. P., Uppala, S. M., Simmons, A. J., Berrisford, P., Poli, P., Kobayashi, S., et al. (2011). The ERA-interim reanalysis: Configuration and performance of the data assimilation system. *Quarterly Journal of the Royal Meteorological Society*, *137*(656), 553–597. https://doi.org/10.1002/qj.828

Desai, N., Diao, M., Shi, Y., Liu, X., & Silber, I. (2023). Ship-based observations and climate model simulations of cloud phase over the southern ocean. *Journal of Geophysical Research: Atmospheres*, *128*(11), e2023JD038581. https://doi.org/10.1029/2023JD038581

Draxl, C., Hahmann, A. N., Peña, A., & Giebel, G. (2014). Evaluating winds and vertical wind shear from Weather Research and Forecasting model forecasts using seven planetary boundary layer schemes. *Wind Energy*, *17*(1), 39–55. https://doi.org/10.1002/we.1555

Duynkerke, P. G., & Teixeira, J. (2001). Comparison of the ECMWF reanalysis with FIRE I observations: Diurnal variation of marine stratocumulus. *Journal of Climate*, *14*(7), 1466–1478. https://doi.org/10.1175/1520-0442(2001)014<1466:COTERW>2.0.CO;2

European Centre for Medium-Range Weather Forecasts. (2009). ERA-interim project [Dataset]. *European Centre for Medium-Range Weather Forecasts*. https://doi.org/10.5065/D6CR5RD9

Field, P. R., Cotton, R. J., McBeath, K., Lock, A. P., Webster, S., & Allan, R. P. (2014). Improving a convection-permitting model simulation of a cold air outbreak. *Quarterly Journal of the Royal Meteorological Society*, *140*(678), 124–138. https://doi.org/10.1002/qj.2116

Finger, J. E., & Wendling, P. (1990). Turbulence structure of arctic stratus clouds derived from measurements and calculations. *Journal of the Atmospheric Sciences*, *47*(11), 1351–1373. https://doi.org/10.1175/1520-0469(1990)047<1351:Tsoasc>2.0.Co;2

Furtado, K., & Field, P. (2017). The role of ice microphysics parametrizations in determining the prevalence of supercooled liquid water in high-resolution simulations of a southern ocean midlatitude cyclone. *Journal of the Atmospheric Sciences*, *74*(6), 2001–2021. https://doi.org/10.1175/JAS-D-16-0165.1

Garcia-Diez, M., Fernandez, J., Fita, L., & Yague, C. (2013). Seasonal dependence of WRF model biases and sensitivity to PBL schemes over Europe. *Quarterly Journal of the Royal Meteorological Society*, *139*(671), 501–514. https://doi.org/10.1002/qj.1976

Ghate, V. P., Miller, M. A., Albrecht, B. A., & Fairall, C. W. (2015). Thermodynamic and radiative structure of stratocumulus-topped boundary layers. *Journal of the Atmospheric Sciences*, *72*(1), 430–451. https://doi.org/10.1175/Jas-D-13-0313.1

Ghonima, M. S., Heus, T., Norris, J. R., & Kleissl, J. (2016). Factors controlling stratocumulus cloud lifetime over coastal land. *Journal of the Atmospheric Sciences*, *73*(8), 2961–2983. https://doi.org/10.1175/JAS-D-15-0228.1

Ghonima, M. S., Yang, H., Kim, C. K., Heus, T., & Kleissl, J. (2017). Evaluation of WRF SCM simulations of stratocumulus-topped marine and coastal boundary layers and improvements to turbulence and entrainment parameterizations. *Journal of Advances in Modeling Earth Systems*, *9*(7), 2635–2653. https://doi.org/10.1002/2017MS001092

Golaz, J.-C., Larson, V. E., & Cotton, W. R. (2002). A PDF-based model for boundary layer clouds. Part II: Model results. *Journal of the Atmospheric Sciences*, *59*(24), 3552–3571. https://doi.org/10.1175/1520-0469(2002)059<3552:APBMFB>2.0.CO;2

Grell, G. A., & Freitas, S. R. (2014). A scale and aerosol aware stochastic convective parameterization for weather and air quality modeling. *Atmospheric Chemistry and Physics*, *14*(10), 5233–5250. https://doi.org/10.5194/acp-14-5233-2014

Hande, L. B., Siems, S. T., Manton, M. J., & Belusic, D. (2012). Observations of wind shear over the Southern Ocean. *Journal of Geophysical Research*, *117*(D12), D12206. https://doi.org/10.1029/2012JD017488

Hannak, L., Knippertz, P., Fink, A. H., Kniffka, A., & Pante, G. (2017). Why do global climate models struggle to represent low-level clouds in the West African summer monsoon? *Journal of Climate*, *30*(5), 1665–1687. https://doi.org/10.1175/JCLI-D-16-0451.1

Hartmann, D. L., Ockert-Bell, M. E., & Michelsen, M. L. (1992). The effect of cloud type on Earth's energy balance: Global analysis. *Journal of Climate*, *5*(11), 1281–1304. https://doi.org/10.1175/1520-0442(1992)005<1281:TEOCTO>2.0.CO;2

Helmis, C. G., Wang, Q., Sgouros, G., Wang, S., & Halios, C. (2013). Investigating the summertime low-level jet over the East Coast of the U.S.A.: A case study. *Boundary-Layer Meteorology*, *149*(2), 259–276. https://doi.org/10.1007/s10546-013-9841-y

Hong, S. Y., Noh, Y., & Dudhia, J. (2006). A new vertical diffusion package with an explicit treatment of entrainment processes. *Monthly Weather Review*, *134*(9), 2318–2341. https://doi.org/10.1175/Mwr3199.1

Hu, X.-M. (2025). Outputs of WRF simulations over Southern Ocean [Dataset]. *WRF*. Retrieved from https://caps.ou.edu/micronet/SouthernOcean.html

Hu, X.-M., Doughty, D. C., Sanchez, K. J., Joseph, E., & Fuentes, J. D. (2012). Ozone variability in the atmospheric boundary layer in Maryland and its implications for vertical transport model. *Atmospheric Environment*, *46*, 354–364. https://doi.org/10.1016/j.atmosenv.2011.09.054

Hu, X.-M., Huang, Y., Xue, M., Martin, E., Hong, Y., Chen, M., et al. (2023). Effects of lower troposphere vertical mixing on simulated clouds and precipitation over the Amazon during the wet season. *Journal of Geophysical Research: Atmospheres*, *128*(12), e2023JD038553. https://doi.org/10.1029/2023JD038553

Hu, X.-M., Klein, P. M., & Xue, M. (2013). Evaluation of the updated YSU planetary boundary layer scheme within WRF for wind resource and air quality assessments. *Journal of Geophysical Research-Atmospheres*, *118*(18), 10490–10505. https://doi.org/10.1002/jgrd.50823

Hu, X.-M., McFarquhar, G., Wu, W., & Xue, M. (2021). Three modes of cloud-boundary layer coupling over the southern ocean: Performance of conventional and mass-flux PBL schemes. In *Paper presented at the AGU Fall Meeting*. Retrieved from https://agu2021fallmeeting-agu.ipostersessions.com/?s=FE-29-A2-50-FF-3B-DE-5B-62-93-85-2F-4C-B5-CA-09

Hu, X.-M., Nielsen-Gammon, J. W., & Zhang, F. Q. (2010). Evaluation of three planetary boundary layer schemes in the WRF model. *Journal of Applied Meteorology and Climatology*, *49*(9), 1831–1844. https://doi.org/10.1175/2010jamc2432.1

Hu, X.-M., Xue, M., & Li, X. (2019). The use of high-resolution sounding data to evaluate and optimize nonlocal PBL schemes for simulating the slightly stable upper convective boundary layer. *Monthly Weather Review*, *147*(10), 3825–3841. https://doi.org/10.1175/MWR-D-19-0085.1

Hu, X.-M., Zhang, F., Yu, G., Fuentes, J. D., & Wu, L. (2011). Contribution of mixed-phase boundary layer clouds to the termination of ozone depletion events in the Arctic. *Geophysical Research Letters*, *38*(21). https://doi.org/10.1029/2011gl049229

Hu, Y., Lebo, Z. J., Geerts, B., Wang, Y., & Hu, Y. (2023). Vertical structure and ice production processes of shallow convective postfrontal clouds over the southern ocean in MARCUS. Part II: Modeling study. *Journal of the Atmospheric Sciences*, *80*(5), 1307–1327. https://doi.org/10.1175/JAS-D-21-0272.1

Huang, H. Y., Hall, A., & Teixeira, J. (2013). Evaluation of the WRF PBL parameterizations for marine boundary layer clouds: Cumulus and stratocumulus. *Monthly Weather Review*, *141*(7), 2265–2271. https://doi.org/10.1175/Mwr-D-12-00292.1

Huang, Y., Franklin, C. N., Siems, S. T., Manton, M. J., Chubb, T., Lock, A., et al. (2015). Evaluation of boundary-layer cloud forecasts over the Southern Ocean in a limited-area numerical weather prediction system using, space-borne and ground-based observations. *Quarterly Journal of the Royal Meteorological Society*, *141*(691), 2259–2276. https://doi.org/10.1002/qj.2519

Huang, Y., Siems, S. T., Manton, M. J., & Thompson, G. (2014). An evaluation of WRF simulations of clouds over the southern ocean with a-train observations. *Monthly Weather Review*, *142*(2), 647–667. https://doi.org/10.1175/MWR-D-13-00128.1

Hyder, P., Edwards, J. M., Allan, R. P., Hewitt, H. T., Bracegirdle, T. J., Gregory, J. M., et al. (2018). Critical Southern Ocean climate model biases traced to atmospheric model cloud errors. *Nature Communications*, *9*(1), 3625. https://doi.org/10.1038/s41467-018-05634-2

Iacono, M. J., Delamere, J. S., Mlawer, E. J., Shephard, M. W., Clough, S. A., & Collins, W. D. (2008). Radiative forcing by long-lived greenhouse gases: Calculations with the AER radiative transfer models. *Journal of Geophysical Research*, *113*(D13). https://doi.org/10.1029/2008JD009944

Jakob, C. (1999). Cloud cover in the ECMWF reanalysis. *Journal of Climate*, *12*(4), 947–959. https://doi.org/10.1175/1520-0442(1999)012<0947:CCITER>2.0.CO;2

Janjic, Z. I. (1990). The step-mountain coordinate: Physical package. *Monthly Weather Review*, *118*(7), 1429–1443. https://doi.org/10.1175/1520-0493(1990)118<1429:TSMCPP>2.0.CO;2

Jensen, J. B., Lee, S., Krummel, P. B., Katzfey, J., & Gogoasa, D. (2000). Precipitation in marine cumulus and stratocumulus: Part I: Thermodynamic and dynamic observations of closed cell circulations and cumulus bands. *Atmospheric Research*, *54*(2), 117–155. https://doi.org/10.1016/S0169-8095(00)00040-5

Jiménez, P. A., Dudhia, J., González-Rouco, J. F., Navarro, J., Montávez, J. P., & García-Bustamante, E. (2012). A revised scheme for the WRF surface layer formulation. *Monthly Weather Review*, *140*(3), 898–918. https://doi.org/10.1175/mwr-d-11-00056.1

Jones, C. R., Bretherton, C. S., & Leon, D. (2011). Coupled vs. decoupled boundary layers in VOCALS-REx. *Atmospheric Chemistry and Physics*, *11*(14), 7143–7153. https://doi.org/10.5194/acp-11-7143-2011

Kay, J. E., Wall, C., Yettella, V., Medeiros, B., Hannay, C., Caldwell, P., & Bitz, C. (2016). Global climate impacts of fixing the southern ocean shortwave radiation bias in the Community Earth System Model (CESM). *Journal of Climate*, *29*(12), 4617–4636. https://doi.org/10.1175/JCLI-D-15-0358.1

Klein, P. M., Hu, X.-M., Shapiro, A., & Xue, M. (2016). Linkages between boundary-layer structure and the development of nocturnal low-level jets in central Oklahoma. *Boundary-Layer Meteorology*, *158*(3), 383–408. https://doi.org/10.1007/s10546-015-0097-6

Lang, F., Ackermann, L., Huang, Y., Truong, S. C. H., Siems, S. T., & Manton, M. J. (2022). A climatology of open and closed mesoscale cellular convection over the Southern Ocean derived from Himawari-8 observations. *Atmospheric Chemistry and Physics*, *22*(3), 2135–2152. https://doi.org/10.5194/acp-22-2135-2022

Lang, F., Huang, Y., Protat, A., Truong, S. C. H., Siems, S. T., & Manton, M. J. (2021). Shallow convection and precipitation over the southern ocean: A case study during the CAPRICORN 2016 field campaign. *Journal of Geophysical Research: Atmospheres*, *126*(9), e2020JD034088. https://doi.org/10.1029/2020JD034088

Lang, F., Huang, Y., Siems, S. T., & Manton, M. J. (2018). Characteristics of the marine atmospheric boundary layer over the southern ocean in response to the synoptic forcing. *Journal of Geophysical Research: Atmospheres*, *123*(15), 7799–7820. https://doi.org/10.1029/2018JD028700

Larson, V. E., Schanen, D. P., Wang, M., Ovchinnikov, M., & Ghan, S. (2012). PDF parameterization of boundary layer clouds in models with horizontal grid spacings from 2 to 16 km. *Monthly Weather Review*, *140*(1), 285–306. https://doi.org/10.1175/MWR-D-10-05059.1

Lee, E.-H., Lee, E., Park, R., Kwon, Y. C., & Hong, S.-Y. (2018). Impact of turbulent mixing in the stratocumulus-topped boundary layer on numerical weather prediction. *Asia-Pacific Journal of Atmospheric Sciences*, *54*(1), 371–384. https://doi.org/10.1007/s13143-018-0024-0

LeMone, M. A., Tewari, M., Chen, F., & Dudhia, J. (2013). Objectively determined fair-weather CBL depths in the ARW-WRF model and their comparison to CASES-97 observations. *Monthly Weather Review*, *141*(1), 30–54. https://doi.org/10.1175/MWR-D-12-00106.1

Lilly, D. K. (1968). Models of cloud-topped mixed layers under a strong inversion. *Quarterly Journal of the Royal Meteorological Society*, *94*(401), 292–&. https://doi.org/10.1002/qj.49709440106

Lindenmaier, I., Feng, Y.-C., Bharadwaj, N., Johnson, K., Isom, B., Hardin, J., et al. (2018). Marine W-Band (95 GHz) ARM Cloud Radar (MWACR), 2017-10-29 to 2018-03-24, ARM Mobile Facility (MAR), Hobart, AUS to Antarctic Coast—Resupply ship Aurora Australis; AMF2 (M1) [Dataset]. *Atmospheric Radiation Measurement (ARM) User Facility*. https://doi.org/10.5439/1973911

Liu, S., & Liang, X.-Z. (2010). Observed diurnal cycle climatology of planetary boundary layer height. *Journal of Climate*, *23*(21), 5790–5809. https://doi.org/10.1175/2010JCLI3552.1

Liu, X., Xie, S., Boyle, J., Klein, S. A., Shi, X., Wang, Z., et al. (2011). Testing cloud microphysics parameterizations in NCAR CAM5 with ISDAC and M-PACE observations. *Journal of Geophysical Research*, *116*(D1), D00T11. https://doi.org/10.1029/2011JD015889

Lock, A. P., Brown, A. R., Bush, M. R., Martin, G. M., & Smith, R. N. B. (2000). A new boundary layer mixing scheme. Part I: Scheme description and single-column model tests. *Monthly Weather Review*, *128*(9), 3187–3199. https://doi.org/10.1175/1520-0493(2000)128<3187:Anblms>2.0.Co;2

Mace, G. G., & Protat, A. (2018a). Clouds over the southern ocean as observed from the R/V investigator during CAPRICORN. Part I: Cloud occurrence and phase partitioning. *Journal of Applied Meteorology and Climatology*, *57*(8), 1783–1803. https://doi.org/10.1175/JAMC-D-17-0194.1

Mace, G. G., & Protat, A. (2018b). Clouds over the southern ocean as observed from the R/V investigator during CAPRICORN. Part II: The properties of nonprecipitating stratocumulus. *Journal of Applied Meteorology and Climatology*, *57*(8), 1805–1823. https://doi.org/10.1175/JAMC-D-17-0195.1

Mahrt, L., & Vickers, D. (2002). Contrasting vertical structures of nocturnal boundary layers. *Boundary-Layer Meteorology*, *105*(2), 351–363. https://doi.org/10.1023/A:1019964720989

Mahrt, L., Vickers, D., & Andreas, E. L. (2014). Low-level wind maxima and structure of the stably stratified boundary layer in the coastal zone. *Journal of Applied Meteorology and Climatology*, *53*(2), 363–376. https://doi.org/10.1175/JAMC-D-13-0170.1

McCoy, I. L., Wood, R., & Fletcher, J. K. (2017). Identifying meteorological controls on open and closed mesoscale cellular convection associated with marine cold air outbreaks. *Journal of Geophysical Research: Atmospheres*, *122*(21), 11678–11702. https://doi.org/10.1002/2017JD027031

McFarquhar, G. M., Bretherton, C. S., Marchand, R., Protat, A., DeMott, P. J., Alexander, S. P., et al. (2021). Observations of clouds, aerosols, precipitation, and surface radiation over the southern ocean: An overview of CAPRICORN, MARCUS, MICRE, and SOCRATES. *Bulletin of the American Meteorological Society*, *102*(4), E894–E928. https://doi.org/10.1175/BAMS-D-20-0132.1

Mechem, D. B., Kogan, Y. L., & Schultz, D. M. (2010). Large-eddy observation of post-cold-frontal continental stratocumulus. *Journal of the Atmospheric Sciences*, *67*(10), 3368–3383. https://doi.org/10.1175/2010JAS3389.1

Miller, M. A., & Albrecht, B. A. (1995). Surface-based observations of mesoscale cumulus–stratocumulus interaction during ASTEX. *Journal of the Atmospheric Sciences*, *52*(16), 2809–2826. https://doi.org/10.1175/1520-0469(1995)052<2809:SBOOMC>2.0.CO;2

Morrison, H., & Pinto, J. O. (2006). Intercomparison of bulk cloud microphysics schemes in mesoscale simulations of springtime arctic mixed-phase stratiform clouds. *Monthly Weather Review*, *134*(7), 1880–1900. https://doi.org/10.1175/MWR3154.1

Morrison, H., Thompson, G., & Tatarskii, V. (2009). Impact of cloud microphysics on the development of trailing stratiform precipitation in a simulated squall line: Comparison of one- and two-moment schemes. *Monthly Weather Review*, *137*(3), 991–1007. https://doi.org/10.1175/2008mwr2556.1

Morrison, H., Zuidema, P., Ackerman, A. S., Avramov, A., de Boer, G., Fan, J. W., et al. (2011). Intercomparison of cloud model simulations of Arctic mixed-phase boundary layer clouds observed during SHEBA/FIRE-ACE. *Journal of Advances in Modeling Earth Systems*, *3*(2), M06003. https://doi.org/10.1029/2011ms000066

Muhlbauer, A., McCoy, I. L., & Wood, R. (2014). Climatology of stratocumulus cloud morphologies: Microphysical properties and radiative effects. *Atmospheric Chemistry and Physics*, *14*(13), 6695–6716. https://doi.org/10.5194/acp-14-6695-2014

Nakanishi, M., & Niino, H. (2006). An improved Mellor–Yamada level-3 model: Its numerical stability and application to a regional prediction of advection fog. *Boundary-Layer Meteorology*, *119*(2), 397–407. https://doi.org/10.1007/s10546-005-9030-8

NASA/LARC/SD/ASDC. (2018). SatCORPS CERES GEO edition 4 Himawari-8 Southern Hemisphere version 1.2 [Dataset]. *NASA/LARC/SD/ASDC*. https://doi.org/10.5067/HIM08/CERES/GEO_ED4_SH_V01.2

Nicholls, S. (1984). The dynamics of stratocumulus: Aircraft observations and comparisons with a mixed layer model. *Quarterly Journal of the Royal Meteorological Society*, *110*(466), 783–820. https://doi.org/10.1002/qj.49711046603

Nielsen-Gammon, J. W., Hu, X.-M., Zhang, F., & Pleim, J. E. (2010). Evaluation of planetary boundary layer scheme sensitivities for the purpose of parameter estimation. *Monthly Weather Review*, *138*(9), 3400–3417. https://doi.org/10.1175/2010mwr3292.1

Nielsen-Gammon, J. W., Powell, C. L., Mahoney, M. J., Angevine, W. M., Senff, C., White, A., et al. (2008). Multisensor estimation of mixing heights over a coastal city. *Journal of Applied Meteorology and Climatology*, *47*(1), 27–43. https://doi.org/10.1175/2007JAMC1503.1

Nielsen-Gammon, J. W., Powell, C. L., Mahoney, M. J., Angevine, W. M., Senff, C., White, A., et al. (2008). Multisensor estimation of mixing heights over a coastal city. *Journal of Applied Meteorology and Climatology*, *47*(1), 27–43. https://doi.org/10.1175/2007jamc1503.1

Noh, Y.-J., Miller, S. D., Heidinger, A. K., Mace, G. G., Protat, A., & Alexander, S. P. (2019). Satellite-based detection of daytime supercooled liquid-topped mixed-phase clouds over the southern ocean using the advanced Himawari imager. *Journal of Geophysical Research: Atmospheres*, *124*(5), 2677–2701. https://doi.org/10.1029/2018JD029524

Olson, J. B., Kenyon, J. S., Angevine, W. A., Brown, J. M., Pagowski, M., & Sušelj, K. (2019). A description of the MYNN-EDMF scheme and the coupling to other components in WRF–ARW. https://doi.org/10.25923/n9wm-be49

Olson, J. B., Kenyon, J. S., Djalalova, I., Bianco, L., Turner, D. D., Pichugina, Y., et al. (2019). Improving wind energy forecasting through numerical weather prediction model development. *Bulletin of the American Meteorological Society*, *100*(11), 2201–2220. https://doi.org/10.1175/bams-d-18-0040.1

Papritz, L., Pfahl, S., Sodemann, H., & Wernli, H. (2015). A climatology of cold air outbreaks and their impact on air–sea heat fluxes in the high-latitude South Pacific. *Journal of Climate*, *28*(1), 342–364. https://doi.org/10.1175/JCLI-D-14-00482.1

Pedruzo-Bagazgoitia, X., de Roode, S. R., Adler, B., Babić, K., Dione, C., Kalthoff, N., et al. (2020). The diurnal stratocumulus-to-Cumulus transition over land in southern West Africa. *Atmospheric Chemistry and Physics*, *20*(5), 2735–2754. https://doi.org/10.5194/acp-20-2735-2020

Pelucchi, P., Neubauer, D., & Lohmann, U. (2021). Vertical grid refinement for stratocumulus clouds in the radiation scheme of the global climate model ECHAM6.3-HAM2.3-P3. *Geoscientific Model Development*, *14*(9), 5413–5434. https://doi.org/10.5194/gmd-14-5413-2021

Pergaud, J., Masson, V., Malardel, S., & Couvreux, F. (2009). A parameterization of dry thermals and shallow cumuli for mesoscale numerical weather prediction. *Boundary-Layer Meteorology*, *132*(1), 83–106. https://doi.org/10.1007/s10546-009-9388-0

Pichugina, Y. L., & Banta, R. M. (2010). Stable boundary layer depth from high-resolution measurements of the mean wind profile. *Journal of Applied Meteorology and Climatology*, *49*(1), 20–35. https://doi.org/10.1175/2009JAMC2168.1

Pinto, J. O. (1998). Autumnal mixed-phase cloudy boundary layers in the Arctic. *Journal of the Atmospheric Sciences*, *55*(11), 2016–2038. https://doi.org/10.1175/1520-0469(1998)055<2016:Ampcbl>2.0.Co;2

Pleim, J. E. (2007). A combined local and nonlocal closure model for the atmospheric boundary layer. Part I: Model description and testing. *Journal of Applied Meteorology and Climatology*, *46*(9), 1383–1395. https://doi.org/10.1175/Jam2539.1

Priestley, C. H. B., & Swinbank, W. C. (1947). Vertical transport of heat by turbulence in the atmosphere. *Proceedings of the Royal Society of London - Series A: Mathematical and Physical Sciences*, *189*(1019), 543–561. https://doi.org/10.1098/rspa.1947.0057

Qu, X., Hall, A., Klein, S. A., & Caldwell, P. M. (2014). On the spread of changes in marine low cloud cover in climate model simulations of the 21st century. *Climate Dynamics*, *42*(9), 2603–2626. https://doi.org/10.1007/s00382-013-1945-z

Ramadoss, V., Pfannkuch, K., Protat, A., Huang, Y., Siems, S., & Possner, A. (2024). An evaluation of cloud-precipitation structures in mixed-phase stratocumuli over the southern ocean in kilometer-scale ICON simulations during CAPRICORN. *Journal of Geophysical Research: Atmospheres*, *129*(18), e2022JD038251. https://doi.org/10.1029/2022JD038251

Randall, D. A. (1980). Conditional instability of the first kind upside-down. *Journal of the Atmospheric Sciences*, *37*(1), 125–130. https://doi.org/10.1175/1520-0469(1980)037<0125:Ciotfk>2.0.Co;2

Sanchez, K. J., Painemal, D., Brown, M. D., Crosbie, E. C., Gallo, F., Hair, J. W., et al. (2023). Multi-campaign ship and aircraft observations of marine cloud condensation nuclei and droplet concentrations. *Scientific Data*, *10*(1), 471. https://doi.org/10.1038/s41597-023-02372-z

Sandu, I., & Stevens, B. (2011). On the factors modulating the stratocumulus to Cumulus transitions. *Journal of the Atmospheric Sciences*, *68*(9), 1865–1881. https://doi.org/10.1175/2011JAS3614.1

Schuddeboom, A., Varma, V., McDonald, A. J., Morgenstern, O., Harvey, M., Parsons, S., et al. (2019). Cluster-based evaluation of model compensating errors: A case study of cloud radiative effect in the southern ocean. *Geophysical Research Letters*, *46*(6), 3446–3453. https://doi.org/10.1029/2018GL081686

Shapiro, A., & Fedorovich, E. (2010). Analytical description of a nocturnal low-level jet. *Quarterly Journal of the Royal Meteorological Society*, *136*(650), 1255–1262. https://doi.org/10.1002/qj.628

Shin, H. H., & Hong, S.-Y. (2011). Intercomparison of planetary boundary-layer parametrizations in the WRF model for a single day from CASES-99. *Boundary-Layer Meteorology*, *139*(2), 261–281. https://doi.org/10.1007/s10546-010-9583-z

Shin, H. H., & Hong, S. Y. (2015). Representation of the subgrid-scale turbulent transport in convective boundary layers at gray-zone resolutions. *Monthly Weather Review*, *143*(1), 250–271. https://doi.org/10.1175/Mwr-D-14-00116.1

Siebesma, A. P., Soares, P. M. M., & Teixeira, J. (2007). A combined eddy-diffusivity mass-flux approach for the convective boundary layer. *Journal of the Atmospheric Sciences*, *64*(4), 1230–1248. https://doi.org/10.1175/JAS3888.1

Simmonds, I., Keay, K., & Lim, E.-P. (2003). Synoptic activity in the seas around Antarctica. *Monthly Weather Review*, *131*(2), 272–288. https://doi.org/10.1175/1520-0493(2003)131<0272:SAITSA>2.0.CO;2

Skamarock, W. C., & Klemp, J. B. (2008). A time-split nonhydrostatic atmospheric model for weather research and forecasting applications. *Journal of Computational Physics*, *227*(7), 3465–3485. https://doi.org/10.1016/j.jcp.2007.01.037

Skamarock, W. C., Klemp, J. B., Dudhia, J., Gill, D. O., Liu, Z., Berner, J., et al. (2021). A description of the advanced research WRF model version 4.3. (NCAR/TN-556+STR). https://doi.org/10.5065/1dfh-6p97

Smedman, A.-S., Bergström, H., & Högström, U. (1995). Spectra, variances and length scales in a marine stable boundary layer dominated by a low level jet. *Boundary-Layer Meteorology*, *76*(3), 211–232. https://doi.org/10.1007/BF00709352

Smith, W., & Minnis, P. (2020). NASA SatCORPS Himawari cloud retrieval data. Version 2.2 (version 2.2) [Dataset]. https://doi.org/10.5065/D6CC0ZFJ

Soares, P. M. M., Miranda, P. M. A., Siebesma, A. P., & Teixeira, J. (2004). An eddy-diffusivity/mass-flux parametrization for dry and shallow Cumulus convection. *Quarterly Journal of the Royal Meteorological Society*, *130*(604), 3365–3383. https://doi.org/10.1256/qj.03.223

Solomon, A., Shupe, M. D., Persson, P. O. G., & Morrison, H. (2011). Moisture and dynamical interactions maintaining decoupled Arctic mixed-phase stratocumulus in the presence of a humidity inversion. *Atmospheric Chemistry and Physics*, *11*(19), 10127–10148. https://doi.org/10.5194/acp-11-10127-2011

Stevens, B., Acquistapace, C., Hansen, A., Heinze, R., Klinger, C., Klocke, D., et al. (2020). The added value of large-eddy and storm-resolving models for simulating clouds and precipitation. *Journal of the Meteorological Society of Japan. Ser. II*, *98*(2), 395–435. https://doi.org/10.2151/jmsj.2020-021

Stull, R. B. (1988). *An introduction to boundary layer meteorology*. Springer Netherlands.

Sukoriansky, S., Galperin, B., & Perov, V. (2005). Application of a new spectral theory of stably stratified turbulence to the atmospheric boundary layer over sea ice. *Boundary-Layer Meteorology*, *117*(2), 231–257. https://doi.org/10.1007/s10546-004-6848-4

Suselj, K., Kurowski, M. J., & Teixeira, J. (2019). A unified eddy-diffusivity/mass-flux approach for modeling atmospheric convection. *Journal of the Atmospheric Sciences*, *76*(8), 2505–2537. https://doi.org/10.1175/JAS-D-18-0239.1

Suselj, K., Smalley, M., Lebsock, M. D., Kurowski, M. J., Witte, M. K., & Teixeira, J. (2022). Coupling warm rain with an eddy diffusivity/mass flux parameterization: 1. Model description and validation. *Journal of Advances in Modeling Earth Systems*, *14*(8), e2021MS002736. https://doi.org/10.1029/2021MS002736

Tan, Z., Kaul, C. M., Pressel, K. G., Cohen, Y., Schneider, T., & Teixeira, J. (2018). An extended eddy-diffusivity mass-flux scheme for unified representation of subgrid-scale turbulence and convection. *Journal of Advances in Modeling Earth Systems*, *10*(3), 770–800. https://doi.org/10.1002/2017MS001162

Teixeira, J., Cardoso, S., Bonazzola, M., Cole, J., DelGenio, A., DeMott, C., et al. (2011). Tropical and subtropical cloud transitions in weather and climate prediction models: The GCSS/WGNE Pacific Cross-Section Intercomparison (GPCI). *Journal of Climate*, *24*(20), 5223–5256. https://doi.org/10.1175/2011JCLI3672.1

Tian, Y., & Kuang, Z. (2016). Dependence of entrainment in shallow cumulus convection on vertical velocity and distance to cloud edge. *Geophysical Research Letters*, *43*(8), 4056–4065. https://doi.org/10.1002/2016GL069005

Tjernström, M., & Smedman, A.-S. (1993). The vertical turbulence structure of the coastal marine atmospheric boundary layer. *Journal of Geophysical Research*, *98*(C3), 4809–4826. https://doi.org/10.1029/92JC02610

Trenberth, K. E., & Fasullo, J. T. (2010). Simulation of present-day and twenty-first-century energy budgets of the southern oceans. *Journal of Climate*, *23*(2), 440–454. https://doi.org/10.1175/2009JCLI3152.1

Truong, S. C. H., Huang, Y., Lang, F., Messmer, M., Simmonds, I., Siems, S. T., & Manton, M. J. (2020). A climatology of the marine atmospheric boundary layer over the southern ocean from four field campaigns during 2016–2018. *Journal of Geophysical Research: Atmospheres*, *125*(20), e2020JD033214. https://doi.org/10.1029/2020JD033214

Truong, S. C. H., Siems, S. T., May, P. T., Huang, Y., Vignon, É., & Gevorgyan, A. (2023). Characteristics and variability of precipitation across different sectors of an extra-tropical cyclone: A case study over the high-latitudes of the southern ocean. *Journal of Geophysical Research: Atmospheres*, *128*(22), e2023JD039013. https://doi.org/10.1029/2023JD039013

UCAR. (2024). SOCRATES data sets [Dataset]. *UCAR*. Retrieved from https://data.eol.ucar.edu/master_lists/generated/socrates/

van Stratum, B. J. H., Vilá-Guerau de Arellano, J., van Heerwaarden, C. C., & Ouwersloot, H. G. (2014). Subcloud-layer feedbacks driven by the mass flux of shallow Cumulus convection over land. *Journal of the Atmospheric Sciences*, *71*(3), 881–895. https://doi.org/10.1175/JAS-D-13-0192.1

Wang, M., Larson, V. E., Ghan, S., Ovchinnikov, M., Schanen, D. P., Xiao, H., et al. (2015). A multiscale modeling framework model (superparameterized CAM5) with a higher-order turbulence closure: Model description and low-cloud simulations. *Journal of Advances in Modeling Earth Systems*, *7*(2), 484–509. https://doi.org/10.1002/2014MS000375

Wang, S. (1993). Modeling marine boundary-layer clouds with a two-layer model: A one-dimensional simulation. *Journal of the Atmospheric Sciences*, *50*(24), 4001–4021. https://doi.org/10.1175/1520-0469(1993)050<4001:MMBLCW>2.0.CO;2

Wang, S. P., Wang, Q., Jordan, R. E., & Persson, P. O. G. (2001). Interactions among longwave radiation of clouds, turbulence, and snow surface temperature in the Arctic: A model sensitivity study. *Journal of Geophysical Research*, *106*(D14), 15323–15333. https://doi.org/10.1029/2000jd900358

Wang, W. G., Shen, X. Y., & Huang, W. Y. (2016). A comparison of boundary-layer characteristics simulated using different parametrization schemes. *Boundary-Layer Meteorology*, *161*(2), 375–403. https://doi.org/10.1007/s10546-016-0175-4

Wang, Z., Letu, H., Shang, H., & Bugliaro, L. (2024). Technical note: Retrieval of the supercooled liquid fraction in mixed-phase clouds from Himawari-8 observations. *Atmospheric Chemistry and Physics*, *24*(13), 7559–7574. https://doi.org/10.5194/acp-24-7559-2024

Williams, K. D., Bodas-Salcedo, A., Déqué, M., Fermepin, S., Medeiros, B., Watanabe, M., et al. (2013). The transpose-AMIP II experiment and its application to the understanding of southern ocean cloud biases in climate models. *Journal of Climate*, *26*(10), 3258–3274. https://doi.org/10.1175/JCLI-D-12-00429.1

Wilson, T. H., & Fovell, R. G. (2018). Modeling the evolution and life cycle of radiative cold pools and fog. *Weather and Forecasting*, *33*(1), 203–220. https://doi.org/10.1175/Waf-D-17-0109.1

Winker, D. M., Pelon, J., Coakley, J. A., Ackerman, S. A., Charlson, R. J., Colarco, P. R., et al. (2010). The CALIPSO mission: A global 3D view of aerosols and clouds [Dataset]. *Bulletin of the American Meteorological Society*, *91*(9), 1211–1230. https://doi.org/10.1175/2010BAMS3009.1

Wood, R. (2012). Stratocumulus clouds. *Monthly Weather Review*, *140*(8), 2373–2423. https://doi.org/10.1175/MWR-D-11-00121.1

Wyant, M. C., Bretherton, C. S., Rand, H. A., & Stevens, D. E. (1997). Numerical simulations and a conceptual model of the stratocumulus to trade Cumulus transition. *Journal of the Atmospheric Sciences*, *54*(1), 168–192. https://doi.org/10.1175/1520-0469(1997)054<0168:NSAACM>2.0.CO;2

Xi, B., Dong, X., Zheng, X., & Wu, P. (2022). Cloud phase and macrophysical properties over the Southern Ocean during the MARCUS field campaign. *Atmospheric Measurement Techniques*, *15*(12), 3761–3777. https://doi.org/10.5194/amt-15-3761-2022

Xie, B., Fung, J. C. H., Chan, A., & Lau, A. (2012). Evaluation of nonlocal and local planetary boundary layer schemes in the WRF model. *Journal of Geophysical Research*, *117*(D12). https://doi.org/10.1029/2011JD017080

Xu, K.-M., & Cheng, A. (2013). Evaluating low-cloud simulation from an upgraded multiscale modeling framework model. Part I: Sensitivity to spatial resolution and climatology. *Journal of Climate*, *26*(16), 5717–5740. https://doi.org/10.1175/JCLI-D-12-00200.1

Yamaguchi, T., & Randall, D. A. (2012). Cooling of entrained parcels in a large-eddy simulation. *Journal of the Atmospheric Sciences*, *69*(3), 1118–1136. https://doi.org/10.1175/jas-d-11-080.1

Yang, Y., & Gao, S. (2020). The of turbulent diffusion driven by fog-top cooling on sea fog development. *Journal of Geophysical Research: Atmospheres*, *125*(4), e2019JD031562. https://doi.org/10.1029/2019jd031562

Yang, Y., Hu, X.-M., Gao, S., & Wang, Y. (2019). Sensitivity of WRF simulations with the YSU PBL scheme to the lowest model level height for a sea fog event over the Yellow Sea. *Atmospheric Research*, *215*, 253–267. https://doi.org/10.1016/j.atmosres.2018.09.004

Zelinka, M. D., Myers, T. A., McCoy, D. T., Po-Chedley, S., Caldwell, P. M., Ceppi, P., et al. (2020). Causes of higher climate sensitivity in CMIP6 Models. *Geophysical Research Letters*, *47*(1), e2019GL085782. https://doi.org/10.1029/2019GL085782

Zhang, H., Zheng, Y., Lee, S. S., & Li, Z. (2023). Surface-atmosphere decoupling prolongs cloud lifetime under warm advection due to reduced entrainment drying. *Geophysical Research Letters*, *50*(10), e2022GL101663. https://doi.org/10.1029/2022GL101663

Zheng, Y., & Li, Z. (2019). Episodes of warm-air advection causing cloud-surface decoupling during the MARCUS. *Journal of Geophysical Research: Atmospheres*, *124*(22), 12227–12243. https://doi.org/10.1029/2019JD030835

Zheng, Y., Rosenfeld, D., & Li, Z. (2020). A more general paradigm for understanding the decoupling of stratocumulus-topped boundary layers: The importance of horizontal temperature advection. *Geophysical Research Letters*, *47*(14), e2020GL087697. https://doi.org/10.1029/2020GL087697

Zheng, Y., Rosenfeld, D., & Li, Z. (2021). Sub-cloud turbulence explains cloud-base updrafts for shallow cumulus ensembles: First observational evidence. *Geophysical Research Letters*, *48*(6), e2020GL091881. https://doi.org/10.1029/2020GL091881

Zheng, Y., Zhang, H., & Li, Z. (2021). Role of surface latent heat flux in shallow cloud transitions: A mechanism-denial LES study. *Journal of the Atmospheric Sciences*, *78*(9), 2709–2723. https://doi.org/10.1175/JAS-D-20-0381.1

Zheng, Y., Zhang, H., Rosenfeld, D., Lee, S.-S., Su, T., & Li, Z. (2021). Idealized large-eddy simulations of stratocumulus advecting over cold water. Part I: Boundary layer decoupling. *Journal of the Atmospheric Sciences*, *78*(12), 4089–4102. https://doi.org/10.1175/JAS-D-21-0108.1

Zuidema, P., Baker, B., Han, Y., Intrieri, J., Key, J., Lawson, P., et al. (2005). An arctic springtime mixed-phase cloudy boundary layer observed during SHEBA. *Journal of the Atmospheric Sciences*, *62*(1), 160–176. https://doi.org/10.1175/Jas-3368.1